Mechanistic Model of Amine Hydrochloride Salts Precipitation in a Confined Impinging Jet Reactor

# Mechanistic Model of Amine Hydrochloride Salts Precipitation in a Confined Impinging Jet Reactor

Francesco Maluta,[†] Suzanne M. Kresta,[‡] and Alexandra Komrakova[*,¶]

[†]*Department of Industrial Chemistry "Toso Montanari", University of Bologna, Bologna, BO, 40136, Italy*

[‡]*Department of Chemical and Biological Engineering, University of Saskatchewan, Saskatoon, Saskatchewan, S7N 5A9, Canada*

[¶]*Department of Mechanical Engineering, University of Alberta, Edmonton, Alberta, T6G 1H9, Canada*

E-mail: komrakov@ualberta.ca

**Abstract**

A mechanistic model was developed to study the industrial synthesis of the polyurethane precursor, amine hydrochloride, in a confined impinging jet reactor (CIJR). Two chemical reaction steps occur in a competitive-consecutive sequence which results in the precipitation of two amine hydrochloride salts. The formation of the di-amine by-product means loss of starting material and expensive reprocessing of highly insoluble salts. The predictive, mechanistic model includes equations for chemical reaction kinetics, nucleation, particle growth, and the first reported mixing model for the CIJR. In our previous study [Maluta, F. et al. Comput. Chem. Eng. 2017, 106, 322.], we used a full factorial design to determine physically realizable values of the eleven physical constants involved in the model. In this study, we show the importance of using a mixing

model to account for imperfect mixing in the impingement zone. The mixing model treats the impingement zone as a radial jet and resolves the local mixing into 198 discrete compartments. The model was able to predict an unexpected and sudden change in the reaction product distribution as the reactant inlet concentration is increased. Without the local mixing model, it was not possible to replicate this major trend in the experimental results. The local mixing model allows us to determine the conditions under which significant by-product formation will occur. A second industrially important question is whether fine particles or larger particles will be produced. This process outcome was also dominated by local mixing conditions in the impingement region. The model results show a strong influence of local mixing on two key process outcomes.

# Introduction

The synthesis of polyurethane can include a series of undesired side reactions that result in the formation of highly insoluble amine hydrochloride (AHC) salts. The production of these salts means loss of starting material and costly reprocessing of by-product. From an industrial perspective, it is very important to identify conditions when the formation of precipitates is either mitigated or the size of the by-product particles being produced is negligibly small.

The driving force for the precipitation of the AHC salts is their supersaturation. Supersaturation changes as a result of chemical reactions, given constant operating conditions and limited solubility of the reaction products. In a more rigorous sense, supersaturation is a function of the local thermodynamic activity of all compounds and intermediate reaction products. If reactions occur faster than the growth of the precipitated particles, the local supersaturation will increase rapidly, leading to extensive nucleation of fine particles.[1] The rate of supersaturation build-up depends on the reaction kinetics, the local mixing intensity, and concentration of the reacting species, making the control of particle size challenging. As noted by Tung et al.[1] the rate of addition of the reagents does provide a means to control supersaturation globally in the reactor but not locally since reagents may be depleted near the point of addition. High local supersaturation values are relieved by rapid nucleation of small particles. When these particles enter the bulk of the reactor at a lower supersaturation, they grow and reduce the supersaturation even more. The particles can also form hard agglomerates as a result of particle collisions. If every collision led to agglomeration, these agglomerates would reach sizes of microns and larger within seconds.[2] In contrast, small particles/nuclei can also dissolve in the bulk if they are below the critical particle size relative to local supersaturation in the bulk.

Successful operation of precipitation reactors depends on a balance between addition rate of the reagents (local concentration), mixing (local supersaturation), global supersaturation, particle growth rate, inter-particle forces, and local mixing conditions throughout the entire

reactor. Local processes occurring near the feed point are of major importance because in most cases the production of particles takes place in this region. In the specific case of polyurethane synthesis where particle generation is highly undesirable, being able to control the local supersaturation levels will result in better control over the particle species, number and size.

To determine the conditions when precipitation of undesired salts occurs, a simplified reaction scheme was carried out in laboratory experiments.[3] The local mixing conditions near the addition point are well defined in the confined impinging jet reactor (CIJR), which is designed to achieve the high mixing efficiency needed to probe mixing effects. The reacting components are (A side) a liquid mixture of monochlorobenzene (MCB) and 4,4-methylene dianiline (MDA) and (B side) hydrogen chloride dissolved into MCB. On injection of these two mixtures into the opposing inlets of the CIJR and mixing at the impinging point, two chemical reactions occur in a competitive consecutive sequence that results in precipitation of two types of amine hydrochloride salts: methylene dianiline monohydrochloride (or mono-) and methylene dianiline dihydrochloride (or di-). The laboratory experiments by Ershad,[3] carried out at constant room temperature and pressure, proved the existence of these two types of amine hydrochloride salts. The type of the precipitating salt strongly depends on the local concentration of reagents. As the concentration of the reagents in the A side inlet stream increases, there is a rapid shift from di- particle generation to mono- generation. To better understand the reason for this shift, a mechanistic model was developed and validated.

A wide range of models has been proposed to describe precipitation processes in various systems. One of the main differences in the models is the level of resolution of the precipitation environments: from an assumption of a perfectly mixed flow to full resolution of the flow in the reactor. Consideration of a system as perfectly mixed leads to the solution of a population balance equation (PBE) only in order to characterize the size distribution of the precipitates. This approach was implemented in, for instance, early works for batch and semi-batch crystallization of adipic acid[4] and calcium oxalate monohydrate crystals[5] where

the PBE was solved either with the methods of classes or the methods of moments. The focus of these works was mostly to find a reliable and robust way to model complex precipitation processes in which nucleation, growth, agglomeration, and breakage take place.[6]

In cases when the spatial inhomogeneity of the flow and the physical properties of the system substantially affect the precipitation process, the solution of the PBEs must be coupled with models that describe the flow within the reactor in some detail. This can be achieved by dividing the reactor volume into the compartments, i.e. the compartment model approach (CMA) or fully resolving the flow using computational fluid dynamics (CFD).

Several CMA-PBE models exist in the literature to describe precipitation in continuous and semi-batch systems. They use multiple zones to account for the meso-mixing effects due to the injection of reactants. Zauner and Jones[7] used a segregated feed model with one zone for each of the two feed plumes and the third zone representing the bulk to capture the meso-mixing effects. Kresta et al.[8] and Kresta et al.[9] used the Lagrangian-type description of the plume with nine distinct zones. In these works, the PBE was solved only in the bulk of the reactors and not in the feed plumes where nucleation occurred. Schwarzer and Peukert[10] and Schwarzer and Peukert[11] introduced a mixing model based on the engulfment model of micromixing. Their model assumes ideally mixed zones: one containing only feed solution A, one containing only feed solution B, and a contact zone. The contact zone itself consists of two zones, one zone containing only feed solution A, and the mixing zone M containing both solutions. This is a step forward in the description of a segregated plume, but it is limited by an ideally mixed description of the mixing zone that does not allow flow gradients.

A detailed description of the precipitation environment can be achieved through a PBE-CFD coupling. In detail description of turbulent mixing effects is presented by Liu and Fox[12] for consecutive-competitive reactions and Gavi et al.[13] for parallel-competitive reactions. Marchisio[14] expanded the work of Gavi et al.[13] describing the turbulent flow using large eddy simulation modeling. These works do not consider the precipitation process, but paved the way for successive works,[15–17] that included the solution of a PBE to obtain the particle

size distribution of the precipitate in micro-reactors (confined impinging jet reactor, T-mixer, T-confined impinging jet mixer) and also in laboratory-scale stirred tank.[18]

The aim of our model is to explore the interactions of multiple physical processes simultaneously occurring in the reactor: chemical reactions, nucleation, particle growth, and agglomeration. The complexity of this reaction and precipitation system does not allow coupling with the fully resolved fluid flow as obtained, for instance, through a CFD analysis. Therefore, the mathematical description of the flow was reduced to a simplified two-zone flow model combined with a mixing model. In this case, we can still see the effects of mixing on the process results; but, the computational demands of the model are significantly reduced. Our study shows that the mixing model plays a crucial role in the capability of the entire model to replicate a major feature of the experimental results. This means that mixing in CIJR is not perfect and should be accounted for.

A second objective for the model is to understand how the particle size distribution is affected by the local mixing and process conditions. It is necessary to outline the conditions when the formation of the fine particles occur. The behaviour of the particle size distribution was tracked by the solution of the full population balance equations. The description of the physical chemistry, thermodynamics and particle interactions underlying this system is only partially understood. The numerical solution of the system of governing equations is challenging as well. In this paper, we provide a detailed explanation of the PBE model, the governing equations, and the gaps in our knowledge.

The paper is organized as follows: Section 'Experimental system' describes the physical system and the experimental conditions. The detailed model description is given in Section 'Development of the mechanistic model'. The results are discussed in Section 'Results and discussion'. Section 'Conclusions' summarizes the paper and draws several conclusions.

# Experimental system

The experiments[3] carried out prior to the present modelling work were driven by an industrial challenge faced during polyurethane synthesis: a series of undesired side reactions which result in production of sticky particles that cause loss of the starting material and expensive reprocessing. It was first necessary to reproduce the particle precipitation in the lab and identify the conditions under which it occurs.

A confined impinging jet reactor (CIJR) with a volume of 0.125 ml was used to perform the experiments. In this small reactor, two streams emerge from opposing inlets, impinge, mix rapidly, and leave through the outlet as shown in Fig. 1. Full dimensions of the CIJR are given by Siddiqui[19].

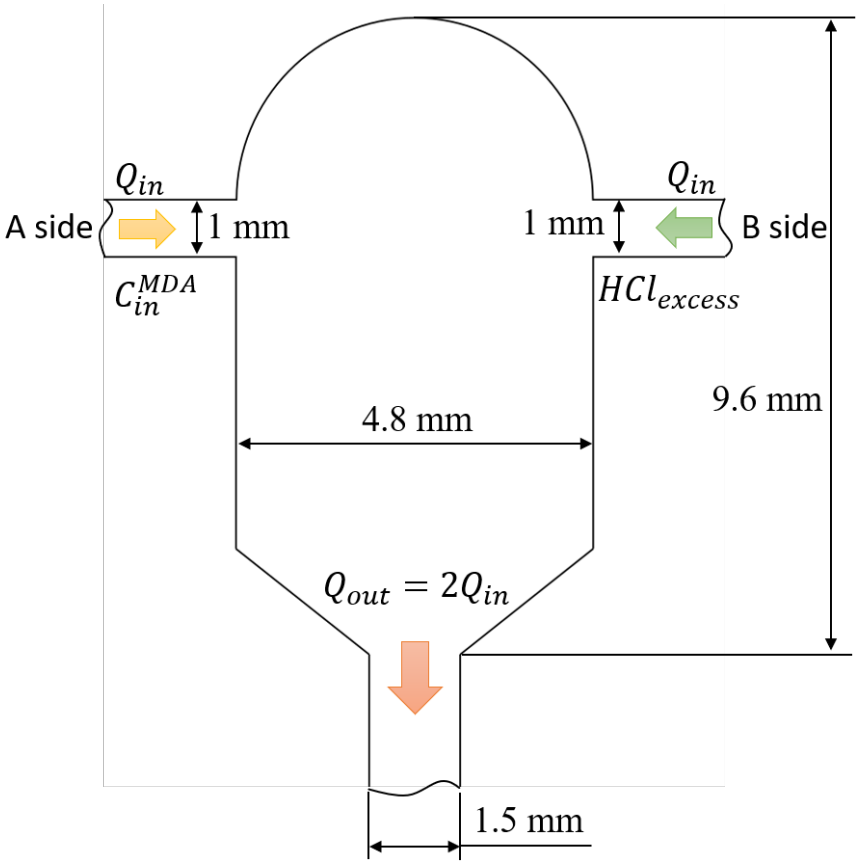


Figure 1: Confined impinging jet reactor (CIJR).

The precipitation of particles in the CIJR occurs in the following way. A liquid mixture

of monochlorobenzene (MCB) and 4,4-methylene dianiline (MDA) characterized by MDA concentration, $C^{in}_{MDA}$, is injected into the left inlet (A side). Hydrogen chloride (HCl) dissolved into MCB is injected into the right inlet in excess of the stoichiometric requirement by $HCl_{excess}$ (B side). As soon as the two streams get mixed down to the molecular level, two chemical reactions take place in a competitive consecutive scheme as follows:

$$MDA + HCl \rightleftarrows MDA.HCl \tag{1a}$$

$$MDA.HCl + HCl \rightleftarrows MDA.2HCl \tag{1b}$$

Inlet flow rates of $Q_{in} = 50$, 100, and 200 ml/min resulting in the inlet Reynolds numbers $Re_{in} = u_{in}d_{in}/\nu$ ($u_{in}$ is the mean velocity in the inlet tube of diameter $d_{in}$ and $\nu$ is the kinematic viscosity of MCB) of 1598, 3196, and 4794, respectively, were tested. The HCl excess is calculated as follows:

$$HCl_{excess} = \frac{\text{Actual injected HCl} - \text{Required HCl (Stoichiometric)}}{\text{Required HCl (Stoichiometric)}} \times 100\%$$

where the stoichiometric value of HCl concentration is twice the corresponding MDA concentration.

When the critical supersaturation of the reaction products in the liquid phase is reached, two types of amine hydrochloride (AHC) salts can precipitate: methylene dianiline monohydrochloride (MDA.HCl) or mono- and methylene dianiline dihydrochloride (MDA.2HCl) or di-. The presence of two types of salts was a significant finding of the experimental project. To determine when and how the formation of particles occurs, several operating conditions were varied: the inlet concentration of MDA, $C^{in}_{MDA}$, referred to as blend strength, inlet excess of HCl, $HCl_{excess}$, and the inlet flow rate of the streams, $Q_{in}$, that was kept equal for both incoming round jets. The overview of the process conditions is given in Table 1. A detailed report of the experiments and analysis of products can be found in Ershad[3].

Table 1: Process conditions for experimental studies

| Blend strength, $C^{in}_{MDA}$ wt % | Inlet flow rate, $Q_{in}$ ml/min | HCl excess, $HCl_{excess}$ % |
|---|---|---|
| 0.5 | | 0 |
| 1.0 | 50 | 100 |
| 2.0 | 100 | 300 |
| 3.5 | 150 | 700 |
| 5.0 | | |

# Development of the mechanistic model

## Model overview

The particle size distribution (PSD) is a result of complex interactions between several processes. To develop a predictive model, careful assessment of each step is required. Following Schwarzer and Peukert [10], a schematic chart of the precipitation process is depicted in Fig. 2.

The AHC salts precipitation process involves multiple interdependent events: mixing, chemical reaction, nucleation, growth, and agglomeration. The flow conditions define the flow field within the device (two impinging round jets in confined geometry). In order to react and produce mono particles the two colliding streams of MDA and HCl solutions have to mix down to the molecular scale. Further reaction of mono- with HCl results in generation of di-particles. Both chemical reactions occur in the liquid phase building up the supersaturation of crystallizing species. When the critical supersaturation is exceeded, the particles nucleate. At the same time, the particles grow and consume supersaturation. Being continuously agitated throughout the reactor, particles collide with each other. Efficient collisions result in the formation of agglomerates.

Supersaturation, nucleation, and growth of particles are strong functions of particle solubility which depends on particle composition and thermodynamic activity. The composition also determines the interfacial tension and inter-particle forces, thus affecting nucleation and agglomeration. The agglomeration rate depends on particle collision rate and colli-

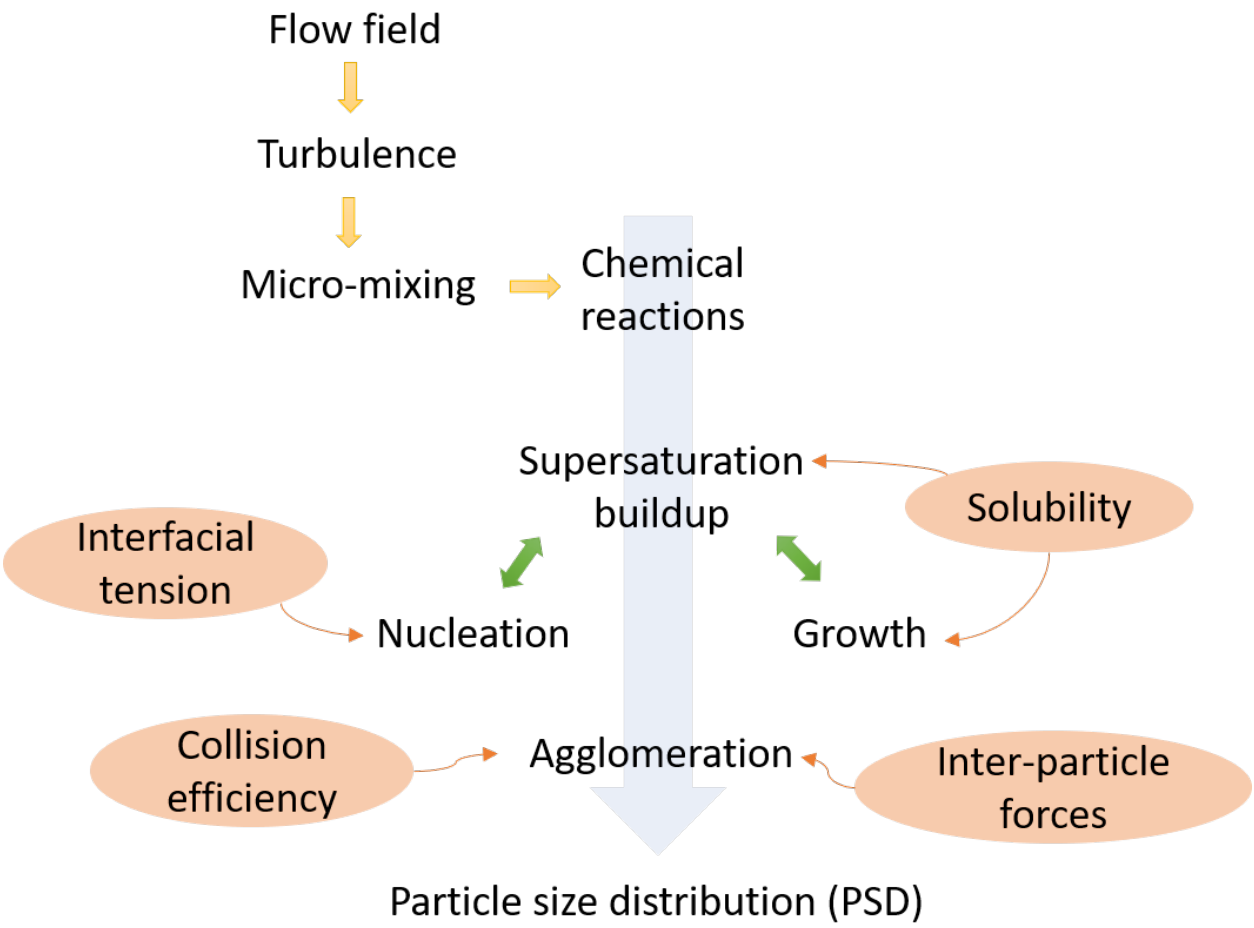


Figure 2: Precipitation of AHC salts in CIJR and the key processes, parameters and properties influencing the particle size distribution.

sion efficiency. The competing time scales of each process also determine the output of the precipitation.

It is important to note that since mixing is not instantaneous, it can affect the rate of chemical reactions. For that reason, the development of a mixing model for the CIJR was of primary importance to success of the mechanistic model. The rate of mixing is directly related to the local turbulence and energy dissipation rates.

The following assumptions are made for the model development:

1. There are no particles at the very beginning of the process which allows us to assume primary nucleation;

2. The density and dynamic viscosity of the mixture are not affected by particles and remain equal to the MCB properties;

3. The fluid flow is not affected by the particles (one-way coupling);

4. Temperature and pressure are maintained constant in the process;

5. Mono- and di- in the liquid phase are generated first (via chemical reactions) building up the supersaturation. Then supersaturation is relieved by simultaneous nucleation and growth;

6. Size-dependent growth is assumed;

7. Binary collisions are assumed for agglomeration;

8. The particles are spherical.

In the experimental campaign, rapid nucleation and agglomeration were observed and no breakage of the AHC salts was reported. Mono- and di- salts had different morphologies and complex shapes. Both agglomeration and particle morphology were set aside in this model. It will be discussed later in the paper, agglomeration affects the size of the particles but does not change the process outcome in terms of the type of particles produced. The uncertainties related to the non-spherical shape of the particles are of secondary importance with respect to other unknowns of the process such as kinetic constants, solubilities, and surface tension.

The governing equations for the mechanistic model are presented below.

## Mixing model

It has been clearly shown by numerous experimental and numerical studies[2,10,11,24] that mixing plays a major role in the precipitation process, significantly affecting the final particle size distribution. In the confined impinging jet reactor the relevant mixing scales are meso-mixing at scales between the inlet pipe diameter and the intermediate eddy size; and micro-mixing down to the molecular level where chemical reactions occur. Even though the CIJR

is characterized by a more uniform distribution of energy dissipation rate than conventional stirred tanks,[25] the local rate of energy dissipation in the area of impingement is significantly higher than in the bulk of the reactor. For that reason, the reactor is split into two zones with different mean mixing intensities and flow model equations as shown in Fig. 3.

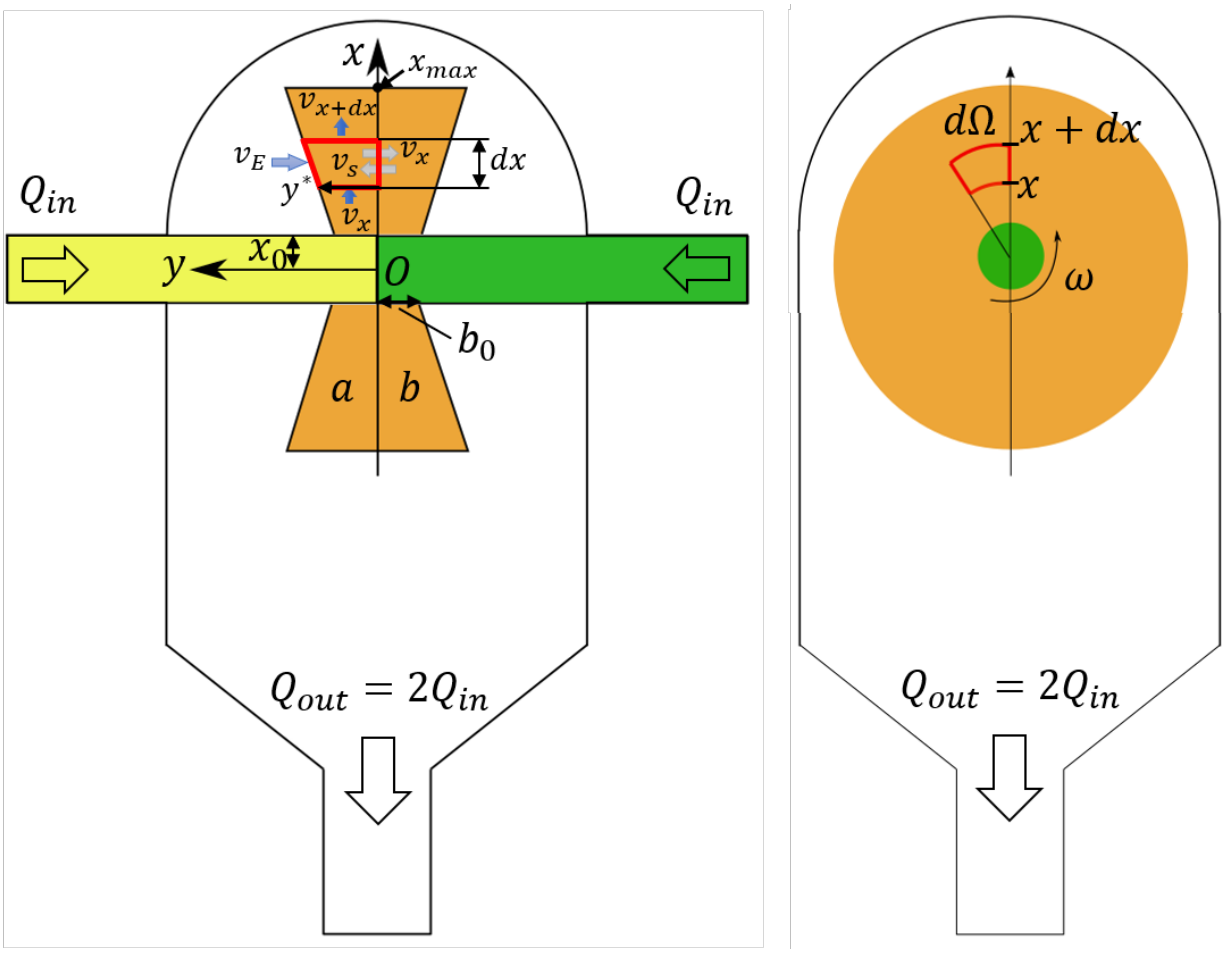


Figure 3: Flow model schematic (not to scale). The impinging round jets are colored in yellow and green, the radial jet is colored in orange. Left: front view of the radial jet; Right: side view of the radial jet. The differential control volume is shown in red.

The mixing model was defined based on the CFD analysis of the flow in a CIJR.[12,14,19,35] Two round jets enter the reactor volume from the nozzles on opposite sides of the reactor, they collide and produce a radial jet perpendicular to the round jets. The modelled CIJR is divided in two zones: the radial jet (orange color) produced by the impinging round jets and the bulk (white color), which is the rest of the fluid volume. The volume occupied by the

two round jets was neglected, since it is only 3.02% of the total volume, as shown in Table 2. The radial jet is assumed to be two-dimensional in $(x - y)$ plane and axisymmetric in the third dimension ($\omega$-coordinate). The radial jet is assumed to mix rapidly and dissipate into the bulk of the reactor before it reaches the walls, thus in Fig. 3 it is shown not reaching the walls.

Table 2: Volumes of the reactor zones.

| Zone | Volume, [$m^3$] | Percentage of the total volume |
|---|---|---|
| Reactor | $1.25 \cdot 10^{-7}$ | 100.00% |
| Radial Jet | $2.28 \cdot 10^{-8}$ | 18.20% |
| Round Jets | $3.77 \cdot 10^{-9}$ | 3.02% |
| Bulk | $9.85 \cdot 10^{-8}$ | 78.78% |

Perfect mixing is assumed in the bulk zone of the reactor, meaning that, in the entire volume of this zone, the species concentration, and the turbulent energy dissipation rate are spatially uniform.

In the radial jet, the variables change as the fluids move away (downstream) from the impingement region of the two round jets, both in the downstream and in the radial jet width directions. At the beginning of the simulation, the bulk concentration is zero for all species. The reactants are introduced in the reactor through the round jets. The radial jet fluid dynamics is modelled at the steady state, so the formation of the radial jet occurs instantaneously. As the reactants travel downstream in the radial jet, the reaction products are continuously discharged from the radial jet into the bulk and the bulk fluid is engulfed into the radial jet. Hence, the species concentration in the bulk and in the radial jet change with time. Furthermore, the radial jet and the bulk are connected by means of an engulfment stream that flows from the bulk to the radial jet and determines the downstream increase in the radial jet volume. The engulfment flow rate is constant with time, whereas the concentration of the species transported can change due to changes in the bulk concentration. All the components eventually leave the reactor through the outlet pipe. The reactor reaches

steady state when there are no further changes with time.

### Mass balance and mixing model in the radial jet

We determined the volume of the radial jet by a differential global mass balance in the radial jet zone (Fig. 3)

$$\frac{d(\rho V)}{dt} = (\rho \dot{V})_x - (\rho \dot{V})_{x+dx} + (\rho\, d\dot{V})_E + (\rho\, d\dot{V})_S - (\rho\, d\dot{V})_S \tag{2}$$

where $V$ is the volume of the differential element or control volume (in red boundaries, in Fig. 3), $\rho$ is the fluid density, $\left(\rho \dot{V}\right)_x$ is the mass flow rate entering the control volume, $\left(\rho \dot{V}\right)_{x+dx}$ is the mass flow rate exiting the control volume (white arrows in Fig. 3), $\left(\rho\, d\dot{V}\right)_E$ is the differential entrainment mass flow rate (blue arrow in Fig. 3), and $\left(\rho\, d\dot{V}\right)_S$ are the differential exchange mass flow rates between the compartments (green arrows). Equation (2) can be simplified assuming steady state, constant density, and the fact that the flow rates between the compartments are of equal magnitude from one side to another, resulting in the following equation:

$$d\dot{V} = \dot{V}_{x+dx} - \dot{V}_x = d\dot{V}_E \tag{3}$$

The downstream volumetric flow rate can be written as:

$$\dot{V}(x) = 2 \int_0^{2\pi} x d\Omega \int_0^{y^*(x)} v_x(x, y) dy \tag{4}$$

with $d\Omega$ being the depth of the control volume along the $\omega$ axis (Fig. 3), $y^*(x)$ the width of the radial jet at the $x$ position (black arrow at the beginning of the control volume, in Fig. 3) and $v_x(x, y)$ is the velocity in the $x$-direction. For the derivation of eq. (4) we assumed all properties constant along $\omega$ axis.

The engulfment flow rate is calculated as:

$$\dot{V}_E = 2\int_0^{2\pi} x d\Omega \int_{x_0}^{x_{max}} v_E dx \tag{5}$$

where $x_{max}$ is the outer radius of the radial jet.

As before, we assumed all properties constant along $\omega$ axis, engulfment velocity, $v_E$, constant along the concave differential surface of the control volume and perpendicular to $dx$ ($v_E \times dy = 0$).

Assuming that the differential exchange volumetric flow rate, $d\dot{V}_S$, is perpendicular to $dx$ and has the same magnitude in both direction ($a \rightarrow b$ equals $a \leftarrow b$), we can write:

$$\dot{V}_S = \int_0^{2\pi} x d\Omega \; v_S dx \tag{6}$$

with $v_S$ being the exchange velocity, defined as a fraction $Z$ of the engulfment velocity $v_E$, eq. (7).

$$v_S = Z \cdot v_E \tag{7}$$

Substituting eq. (4) and (5) into eq. (3) and applying Leibniz's rule for differentiation under the integral sign, we obtain eq. (8a). Since it was assumed that the confined geometry limits the expansion of the radial jet, the derivative $\dfrac{dy^*(x)}{dx}$ is known. The engulfment velocity can be calculated by rearranging eq. (8a) into eq. (8b).

$$\frac{dy^*}{dx} = \frac{v_E - \int_0^{y^*(x)} \dfrac{\partial v_x}{\partial x} dy}{v_x(x, y^*)} \tag{8a}$$

$$v_E = \frac{dy^*}{dx} v_x(x, y^*) + \int_0^{y^*} \frac{\partial v_x}{\partial x} dy \tag{8b}$$

Equations (8) provide an expression for the downstream radial jet expansion, once an $x-$velocity profile is defined.

In the same control volume, named '$a$', the mass balance for the generic $i^{th}$ species was derived. The other compartment was named '$b$'. Assuming volumetric reaction, the species mass balance in the radial jet compartment '$a$' with volume $dV$ reads:

$$\frac{d(C_i dV)_a}{dt} = (C_i \dot{V})_{a,x} - (C_i \dot{V})_{a,x+dx} + (\dot{n}'''_{i,g} dV)_a + (C_{i,E} \dot{V}_E)_a + (C_{i,b} - C_{i,a})\dot{V}_S \tag{9}$$

where $C_i$ is the molar concentration of the $i^{th}$ component, $(C_i \dot{V})_{a,x}$ is the molar flow rate of the $i^{th}$ component entering the compartment $a$, $(C_i \dot{V})_{a,x+dx}$ is the molar flow rate of the $i^{th}$ component exiting the compartment $a$, $(C_{i,E} \dot{V}_E)_a$ is the molar flow rate of the $i^{th}$ component engulfed in $a$, $C_{i,a}$ and $C_{i,b}$ are the molar concentration of $i^{th}$ component in compartments $a$ and $b$, respectively, and $(\dot{n}'''_{i,g} dV)_a$ is the reaction term in the compartment $a$. The notation $\dot{n}_{i,g}$ indicates the rate of generation of $i^{th}$ component [kmol$\cdot$s$^{-1}$], consequently, $\dot{n}'''_{i,g}$ represents the same quantity per unit volume [kmol $\cdot$ s$^{-1}$ $\cdot$ m$^{-3}$].

The differential volume of the compartment $a$, $dV_a$, is equal to:

$$dV_a = y^* dx \int_0^{2\pi} x d\Omega \tag{10}$$

Substituting equations (4), (5), (6) and (10) into equation (9) and writing it at the steady state $\left(\frac{d(C_i dV)_a}{dt} = 0\right)$ we find:

$$\frac{d}{dx}\Big(C_{i,a} \int_0^{y^*(x)} v_x dy\Big) = C_{i,E} v_E + \dot{n}'''_{i,g} y^* + (C_{i,b} - C_{i,a}) v_S \tag{11}$$

Applying Leibniz's rule for differentiation under the integral sign we obtain:

$$\frac{dC_{i,a}}{dx} = \frac{(C_{i,E} - C_{i,a}) v_E + (C_{i,b} - C_{i,a}) v_S + \dot{n}'''_{i,g} y^*}{\int_0^{y^*(x)} v_x dy} \tag{12}$$

This is the equation that describes the evolution of the concentrations of the species along the downstream coordinate of the radial jet. Eq.12 is solved numerically for each side (a

and b) by discretizing the $x-$axis into 99 compartments. It should be highlighted that the term $C_{i,E}$ depends on the reactant concentration in the bulk, which is time dependent. The steady state hypothesis is assumed to describe the fluid dynamics of the radial jet, whereas the species concentrations change in time.

**Species balance in the bulk**

The equations that describe the changes in time of species concentration in the bulk are derived in this section. The mass of the species in the bulk changes due to the discharge from the radial jet, the engulfment from the bulk to the radial jet, the outflow from the reactor, the reactions, and the precipitation. Thus, the mass balance for the bulk zone reads:

$$\frac{d(C_i V_{bulk})}{dt} = \dot{V}_e C_{i,e} - \dot{V}_E C_i - \dot{V}_u C_i + \dot{n}'''_{i,g} V_{bulk} \tag{13}$$

where $C_i$ is the concentration of the $i^{th}$ component in the bulk, $V_{bulk}$ is the volume of the bulk, $\dot{V}_u$ is the volumetric flow rate exiting the reactor, $\dot{V}_e$ is the volumetric flow rate at the end of the radial jet. Therefore $\dot{V}_e C_{i,e}$ is the molar flow rate of the $i^{th}$ component discharged by the radial jet in the bulk, moreover:

$$\dot{V}_e = \dot{V}_u + \dot{V}_E \tag{14}$$

We can rewrite eq. (13):

$$\frac{dC_i}{dt} = \frac{C_{i,e} - C_i}{\tau_{bulk}} + \dot{n}'''_{i,g} \tag{15}$$

where we defined $\tau_{bulk}$ as the residence time in the bulk which is equal to

$$\tau_{bulk} = \frac{V_{bulk}}{\dot{V}_e} \tag{16}$$

**Constitutive equations for the radial jet velocity**

Once the governing equations are derived, an expression for the velocity in the $x$ (downstream) direction in the radial jet zone should be outlined. A 2D model for free turbulent radial jets in the vicinity of its origin (i.e. for small $x$) is used[26] to calculate the velocity

$$v_x = \sqrt{\frac{3K_e}{8\pi x_0}}\sigma_0 \frac{1}{\sqrt{x - x_0}} \operatorname{sech}^2(\eta) \tag{17}$$

where $x_0$ is the radius of the inlet round jets, $\sigma_0^{-1}$ the initial spreading rate of the turbulent radial jet and $K_e$ the kinematic momentum flux which is equal to

$$K_e = 4\pi x_0 \int_0^\infty v_x^2 dy = const = 4\pi x_0 b_0 v_0^2 \tag{18}$$

where $b_0$ is the initial half width of the radial jet and $v_0$ is obtain dividing the inlet volumetric flow rate (Fig. 3, $Q_{tot,in} = 2Q_{in}$), by the impingement area:

$$v_0 = \frac{Q_{tot,in}}{2\pi x_0 \cdot 2b_0} \tag{19}$$

According to[26], the initial spreading rate of the turbulent radial free jet is identical to that of the two-dimensional turbulent plane jet for which the spreading constant $\sigma_0$ has been obtained experimentally by Reichardt, see,[27] to be 7.67. $\eta$ is a non-dimensional constant containing both $x$ and $y$, equal to:

$$\eta = \sigma_0 \frac{y}{(x - x_0)} \tag{20}$$

Given these premises, the maximum velocity is

$$v_{x,max} = \sqrt{\frac{3K_e}{8\pi x_0}}\sigma_0 \frac{1}{\sqrt{x - x_0}} \tag{21}$$

and it goes to infinity as $(x - x_0)$ approaches 0. To overcome this singularity, we found

the $x$ coordinate where the maximum $x$-velocity is equal to $v_0$, ($\Delta$), and we defined a new downstream variable (see Fig. 4):

$$x^* = (x - x_0) + \Delta \tag{22}$$

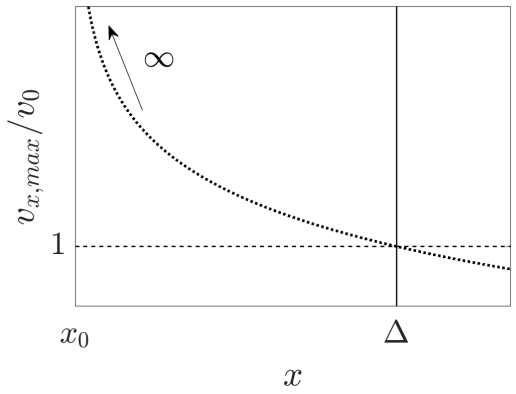


Figure 4: Non dimensional maximum velocity trend and meaning of the constant $\Delta$.

Therefore, the downstream velocity becomes:

$$v_x = \sqrt{1.5 \cdot b_0 \, v_0^2 \, \sigma_0} \, \frac{1}{\sqrt{x^*}} \, \mathrm{sech}^2(\eta) \tag{23}$$

where it should be noted that the $(x - x_0)$ coordinate was used in the expression of $\eta$, instead of the scaled coordinate $x^*$. Since the aforementioned equations were derived for the free radial jet, we imposed a fixed angle of expansion to take the confinement into account: from experimental observations, the expansion angle, $\phi$, was found to be approximately 5°, therefore:

$$y^* = (x - x_0) \cdot \tan(\phi) + b_0 \tag{24}$$

and

$$\frac{dy^*}{dx} = \tan(\phi) \tag{25}$$

It was hypothesized that the confined geometry only affects the $y-$spread of the radial jet, while the maximum $x-$velocity remains the same. Then, it was imposed that, at the edge of the confined radial jet ($y^*$), the $x-$velocity was 1% of the maximum velocity at the corresponding downstream coordinate. Consequently, we defined a new non-dimensional variable, containing both $x$ and $y$, in the same form of $\eta$:

$$\theta = C_1 \frac{y}{x + C_2} = \frac{p}{\tan(\phi)} \frac{y}{\left(x - x_0 + \frac{b_0}{\tan(\phi)}\right)} \tag{26}$$

with $C_1$ and $C_2$ being constants, $p = \text{arcsech}(\sqrt{0.01})$ , so that the $x-$velocity at $y^*$ reads:

$$v_x(x, y^*) = v_{max}\, \text{sech}^2(\theta^*) = v_{max}\, \text{sech}^2 \left( \frac{p}{\tan(\phi)} \frac{(x - x_0)\, \tan(\phi) + b_0}{\left(x - x_0 + \frac{b_0}{\tan(\phi)}\right)} \right) = 0.01\, v_{max} \tag{27}$$

## Coupling of the mixing model and the population balance equation

The mixing model derived above is next coupled with the solution of the population balance equation that describes the evolution of particle size and number. The general form of PBE was modified to take into account the mixing model. Different sets of PBEs were derived for the radial jet and bulk regions.

### Population balance in the radial jet

To model the distribution of states of the solid particles in the radial jet, the population balance equations were derived. A differential control volume over an abstract state space was used. The state space is characterized by the diameter of the solid particles (mono- or di-), $\ell$. According to the classic monodimensional PBE formulation, it was hypothesized that the characteristic diameter increases due to growth and agglomeration, new particles are produced, through nucleation, with the smallest dimension $\ell_0$ (critical nuclei size). The balance was implemented for the generic radial jet semi-compartment, hence particles are constantly convected to and from the semi-compartment. A schematic representation of the

processes through which particles can enter or leave the control volume is shown in Fig. 5.

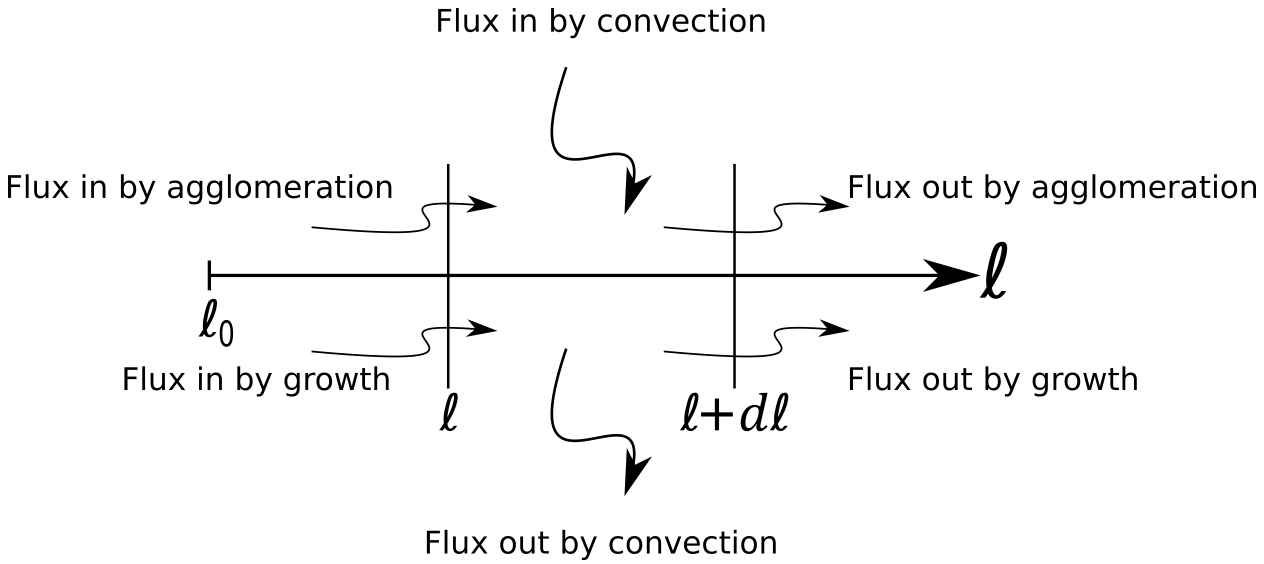


Figure 5: Control volume and fluxes in the $\ell$-space.

Let the distribution we seek be $n_n(\ell)$, $[\#/(\mathrm{m}^3 \cdot \mathrm{m})]$, we defined $n_n(\ell)$ such that: $n_n(\ell)d\ell =$ Number concentration of $n$-particles in the population for which the characteristic diameter takes a value between $\ell$ and $\ell + d\ell$.

The number concentration of $n$-particles inside the differential control volume is $n(\ell_n)_a d\ell_n$ and the particles balance reads:

$$\begin{aligned}\frac{d\left(n_{n,a}(\ell)d\ell\right)}{dt} = &\frac{\left(\dot{V}n_{n,a}(\ell)\right)_x - \left(\dot{V}n_{n,a}(\ell)\right)_{x+dx}}{dV_a}d\ell + \left(G_n n_{n,a}(\ell)\right)_\ell - \left(G_n n_{n,a}(\ell)\right)_{\ell+d\ell} \\ &+ B_{agg,n}d\ell - D_{agg,n}d\ell + \frac{\dot{V}_E}{dV_a}n_{n,E}(\ell)d\ell + \frac{\dot{V}_S}{dV_a}\left(n_{n,b}(\ell) - n_{n,a}(\ell)\right)d\ell\end{aligned} \tag{28}$$

where $dV_a$ indicates the differential volume of the compartment (eq. (10)), $G_n$ is the growth rate of the $n$-particle, $B_{agg,n}$ and $D_{agg,n}$ are respectively the birth and death terms of n-particles due to agglomeration. The last two terms on the right hand side of eq. (28) are the engulfment term and the exchange term; $n_n(\ell)_E d\ell$ and $n_n(\ell)_b d\ell$ are the number concentration of $n$-particles with characteristic diameter between $\ell$ and $\ell + d\ell$ respectively engulfed from the bulk to the semi-compartment $a$ and in the semi-compartment $b$. Writing

eq. (28) at the steady state and simplifying it with the same assumptions used to derive eq. (11), we obtain eq. (29a) that can be rearranged in a form similar to eq. (12)

$$\bar{v}_x(x)\frac{d\,n_{n,a}(\ell)}{dx}+\frac{d\Big(G_n\,n_{n,a}(\ell)\Big)}{d\ell}=B_{agg,n}-D_{agg,n}+\frac{v_E}{y^*}\Big(n_{n,E}(\ell)-n_{n,a}(\ell)\Big)+\frac{v_S}{y^*}\Big(n_{n,b}(\ell)-n_{n,a}(\ell)\Big) \tag{29a}$$

$$\frac{d\,n_{n,a}(\ell)}{dx}+\frac{1}{\bar{v}_x}\frac{d\Big(G_n\,n_{n,a}(\ell)\Big)}{d\ell}=\frac{\Big(n_{n,E}(\ell)-n_{n,a}(\ell)\Big)v_E+\Big(n_{n,b}(\ell)-n_{n,a}(\ell)\Big)v_S+(B_{agg,n}-D_{agg,n})y^*}{\int_0^{y^*(x)}v_x dy} \tag{29b}$$

where $y^*$ is the width of the radial jet, $v_E$ the engulfment velocity, $v_S$ the exchange velocity and $\bar{v}_x$ the y average of the downstream velocity, equal to:

$$\bar{v}_x=\frac{1}{y^*}\int_0^{y^*(x)}v_x dy \tag{30}$$

With the nucleation term the balance becomes:

$$\bar{v}_x(x)\frac{d\,n_{n,a}(\ell)}{dx}+\frac{d\Big(G_n\,n_{n,a}(\ell)\Big)}{d\ell}=B_{agg,n}-D_{agg,n}+\frac{v_E}{y^*}\Big(n_{n,E}(\ell)-n_{n,a}(\ell)\Big)+\frac{v_S}{y^*}\Big(n_{n,b}(\ell)-n_{n,a}(\ell)\Big)+\{B_{nucl,n}\} \tag{31}$$

where $B_{nucl,n}$ is the source term accounting for the nucleation of the $n-$particles. The nucleation term is taken into curved brackets to highlight that this term is relevant to nuclei only - the particles with characteristic dimension between $\ell_0$ and $\ell_0+d\ell$.

Each iteration, the population balance equation (31) is solved in each compartment on both sides of the radial jet, i.e. $99\times2=198$ PBEs are solved in the radial jet. The iterations are repeated until the steady state concentration in the bulk is achieved.

### Population balance in the bulk

Similarly to what was done for the derivation of the PBEs in the radial jet, it was found:

$$\frac{d\,n_n(\ell)}{dt} + \frac{d\Big(G_n\,n_n(\ell)\Big)}{d\ell} = \frac{\Big(n_{n,e}(\ell) - n_n(\ell)\Big)}{\tau_{bulk}} + B_{agg,n} - D_{agg,n} + \{B_{nucl,n}\} \tag{32}$$

with $n_{n,e}(\ell)$ being the $n-$particle density discharged from the end of the radial jet into the bulk. Once again, the nucleation term was only calculated for the $n-$particles with characteristic dimension between $\ell_0$ and $\ell_0 + d\ell$.

## PBE constitutive models

The PBEs presented in Eq. (31) and Eq.(32) need constitutive models in order to be solved. In this section, the models representing nucleation, growth and agglomeration are presented.

### Nucleation

Following experimental and theoretical predictions of Mersmann[21], primary homogeneous nucleation is assumed to be the dominant mechanism of particle formation at high supersaturations. This assumption is widely applied among researchers to model nucleation for both organic and inorganic species.[10,11,22] The nucleation rate is calculated according to classical nucleation theory:[21]

$$B_{nucl} = 1.5 D_{AB} (C N_A)^{7/3} \sqrt{\frac{\sigma}{k_B T}} \cdot V_m \exp\left[ -\frac{16\pi}{3} \left(\frac{\sigma}{k_B T}\right)^3 \frac{V_m^2}{(\nu_D \ln S)^2} \right] \tag{33}$$

here $B_{nucl}$, $[\mathrm{m}^{-3} \cdot \mathrm{s}^{-1}]$ is the primary homogeneous nucleation rate; $D_{AB}$, $[\mathrm{m}^2 \cdot \mathrm{s}^{-1}]$ is the diffusion coefficient of the supersaturated species of the total concentration $C$, $[\mathrm{kmol} \cdot \mathrm{m}^{-3}]$; $N_A = 6.023 \cdot 10^{26}$ $\mathrm{kmol}^{-1}$ is Avogadro's number; $T = 298$ K is the temperature; $k_B = 1.382 \cdot 10^{-23}$ $\mathrm{J \cdot K}^{-1}$ is Boltzmann constant; $\sigma$, $[\mathrm{N \cdot m}^{-1}]$ is the interfacial tension; $V_m$, $[\mathrm{m}^3]$ is the molecular volume; $\nu_D = 1$ is the dissociation number (set equal to one for non-electrolytes).

The diffusion coefficients were estimated using the Stokes-Einstein relation and their values are equal to $3 \times 10^{-9}$ m$^2$/s for both mono- and di-.

It should be noted that the nucleation rate has a strong dependence on the interfacial tension which appears in the exponential term to the third power. A 20% increase in $\sigma$ results in a decrease in the nucleation rate by several orders of magnitude. Schwarzer and Peukert[11] demonstrated the importance of tracking the interfacial energy of the solid-liquid interface for better prediction of nucleation. Either theoretical predictions as described by Schwarzer and Peukert[11] to calculate $\sigma$ or high quality experimental data is needed.

Since only a rough estimate of $\sigma = 0.02$ N/m for mono- and di- particles is available, in the present study the interfacial tension is calculated using the widely used equation:[21]

$$\frac{\sigma}{k_B T} = K_\sigma (C_C N_A)^{2/3} \ln\left(\frac{C_C}{K}\right) \tag{34}$$

here $C_C$, [kmol/m$^3$] is the molar density of the solid particles, $K$, [kmol$\cdot$m$^{-3}$] is the solubility, and $K_\sigma$ is the interfacial tension constant.

The supersaturation is defined as the ratio between the nucleating species concentration and the species solubility limit:

$$S = \frac{C}{K} \tag{35}$$

The mono- and di- solubility limit values are chosen from the experimental trend domain[20] and they are factor H and I, respectively, in Table 3. The buildup of supersaturation takes place due to chemical reactions which increase $C$, and nucleation occurs when $S$ exceeds the critical supersaturation, $S_{crit}$.

As a result of nucleation, nuclei are produced with the critical nucleus size, $\ell_{crit}$, that can be calculated using the following relation:[21]

$$\ell_{crit} = \frac{4\sigma V_m}{\nu_D k_B T \ \ln(S_{crit})} \tag{36}$$

The critical nucleus size is a highly nonlinear function of supersaturation and interfacial tension. The unknown critical supersaturation for mono- and di- was estimated as $S_{crit} = 1.5$ giving a critical nucleus size of several nanometers.

The concentration change due to nucleation for mono- is given by:

$$\left(\frac{dC}{dt}\right)_{nucl} = B_{nucl} n_{nucl}^{MDA.HCl} \tag{37}$$

where the number of moles of particles is calculated based on the volume of one nucleus: $n_{nucl} = C_C V_{crit}$ with $V_{crit} = \frac{\pi}{6}\ell_{crit}^3$.

**Growth**

In the present study, the growth rate is assumed to be mass transfer limited due to the relatively high supersaturation levels typical of precipitation reactions. The growth rate is calculated as follows:[21]

$$G\big(\ell, S(t)\big) = \frac{\partial \ell}{\partial t} = 2\frac{\mathrm{Sh} \cdot D_{AB} \cdot K}{C_C}\frac{S-1}{\ell} \tag{38}$$

where Sh is the Sherwood number (dimensionless mass transfer coefficient) of the particles.

The concentration change due to growth is calculated as follows:

$$\left(\frac{dC}{dt}\right)_{growth} = 3k_v C_C \int_{\ell_{min}}^{\ell_{max}} \ell^2(t) n(\ell, t) G(\ell, t) d\ell \tag{39}$$

where $n(\ell, t)$ is the number density, $G(\ell, t)$ is the growth rate, and $k_v$ is the shape factor.

**Agglomeration**

Agglomeration of particles due to binary collision is modelled for two collision mechanisms:[11,21] collisions resulting from random Brownian motion, termed 'perikinetic', and shear-induced collisions, termed 'orthokinetic'. For perikinetic aggregation, the collision

rate can be calculated according to eq. (40a), while for orthokinetic aggregation eq. (40b) is applied.

$$\beta_{coll,peri} = \frac{2k_B T}{3\mu}\frac{(\ell+\lambda)^2}{\ell\lambda} \tag{40a}$$

$$\beta_{coll,ortho} = \sqrt{\frac{8\pi}{15}}(\ell+\lambda)^3\sqrt{\frac{\epsilon}{\nu}} \tag{40b}$$

where $\ell$ and $\lambda$ are the sizes of the two colliding particles, and $\epsilon$ is the energy dissipation rate.

The collision kernel used in the PBE is the sum of two kernels $\beta_{coll} = \beta_{coll,peri} + \beta_{coll,ortho}$. In order to obtain the agglomeration kernel, it is necessary to multiply the collision frequency by the agglomeration efficiency, $\alpha(\ell,\lambda)$, which describes the probability that a collision is successful and is determined by the particle interaction forces:

$$\beta_{agg}(\ell,\lambda) = \beta_{coll}(\ell,\lambda)\alpha(\ell,\lambda) \tag{41}$$

In this study, the collision efficiency was held constant and equal to 1 meaning that every collision results in agglomeration. This assumption provides the worst case scenario where particles agglomerate rapidly and form large agglomerates. A complete model would need to estimate interparticle forces in order to quantify the agglomeration efficiency more accurately.[11,15,22,23]

It is expected that in moderate turbulent conditions the agglomeration of particles, particularly those at the scale of nuclei, will be dominated by the perikinetic mechanism. In highly turbulent flows such as the impingement point in a CIJR, shear-induced agglomeration can also have an effect, especially for larger particles. Both collision kernels should be considered due to variation of flow conditions in CIJR and the rapid growth of particles.

## Summary

Once the model was developed, values for eleven factors (nine physical constants and two model parameters) were required. A full factorial design search on the model highlighted the factors that have the highest impact on precipitation in the CIJR and narrowed down the range of reported literature values for the full set of physical constants to those which would yield physically meaningful model outcomes.[20] The eleven factors and the values determined from the previous study are presented in Table 3.

Table 3: Model constants and their unoptimized best value from the full factorial design search

| | Factor | Symbol | Value | Units | Equation |
|---|---|---|---|---|---|
| Expansion angle of the jet | A | $\phi$ | 5.0 | $^o$ | Eq.24 |
| Initial half width of the jet | B | $b_0$ | $2.0 \cdot 10^{-4}$ | m | Eq.18 |
| Coefficient for the exchange velocity | C | $Z$ | 1% | $\%V_E$ | Eq.7 |
| Equilibrium constant for reaction 1 | D | $K^{-1}_{mono-,eq}$ | $5.0 \cdot 10^{-5}$ | $\mathrm{kmol \cdot m^{-3}}$ | Eq.1a |
| Equilibrium constant for reaction 2 | E | $K^{-1}_{di-,eq}$ | $1.0 \cdot 10^{-5}$ | $\mathrm{kmol \cdot m^{-3}}$ | Eq.1b |
| Reverse reaction rate for reaction 1 | F | $k_{mono-,r}$ | 0.1 | $s^{-1}$ | Eq.1a |
| Reverse reaction rate for reaction 2 | G | $k_{di-,r}$ | $5.0 \cdot 10^{-3}$ | $s^{-1}$ | Eq.1b |
| Solubility of mono- | H | $K_{mono-}$ | $5.0 \cdot 10^{-7}$ | %mol | Eq.35 |
| Solubility of di- | I | $K_{di-}$ | $1.0 \cdot 10^{-11}$ | %mol | Eq.35 |
| Coefficient for the surface tension of mono- | J | $K_{\sigma,mono-}$ | 0.37 | [−] | Eq.34 |
| Coefficient for the surface tension of di- | K | $K_{\sigma,di-}$ | 0.33 | [−] | Eq.34 |

It should be noted that the factors in Table 3 are not optimized or tuned to fit the experiments. This set of factors was chosen in a previous work[20] from a domain in which for any combination of the factors, the predictive model can reproduce the experimentally observed trends. No attempts to improve the agreement of the model results with the experimental data were made since the goal of the model was to reproduce the experimental trends and uncover the dominant mechanisms driving by-product formation. This set of factors is used for all simulations. The full factorial design[20] was performed for the pure growth, i.e. agglomeration of particles was neglected. Inclusion of agglomeration results requires at least two more constants − the agglomeration efficiencies $\alpha$ (see eq. (41)) for

mono- and di- in addition to those in Table 3. The choice of these constants is not trivial and goes beyond the scope of this study.

## Discretization of the population balance equations

The systems of equations (12) and (15) that describe evolution of concentration of species in radial jet compartments and in the bulk, respectively, should be discretized in time only. The fourth-order Runge-Kutta method (RK4) is used. The fixed time step is used which value is based on stability requirements of the PBE solution.

The population balance equations (31) and (32) were discretized using high resolution schemes for the growth term and the pivot method by Kumar and Ramkrishna[6] was used to discretize the agglomeration terms. This idea was originally proposed by Vale and McKenna[28] and then successfully used by Gunawan et al.[29]. It was demonstrated by Gunawan et al.[29] and then confirmed by Bouaswaig and Engell[30] that the high-resolution methods significantly reduce the numerical diffusion associated with low order methods and avoid spurious oscillations that are observed when higher order methods are used.

Hyperbolic nature of the PBEs along with sharp gradients of the particle size distribution make the solution of this equations challenging. Hermanto et al.[31] showed that first-order methods require small bin size to mitigate numerical diffusion (i.e., smearing); while higher order methods introduce numerical dispersion (i.e., spurious oscillations), leading to negative values of particle size distribution. The computational methods used to solve the population balance equations must be sufficiently accurate to ensure that the behaviour of the numerical solution is not affected by the choice of the numerical method. At the same time, the simulations need to be efficient in terms of computational demands. A conservative finite difference scheme is used in this study to solve the PBE.[32–34] The details of the discretization of population balance equations are given in Supporting information. Verification and validation of the numerical scheme can also be found in Supporting material.

# Results and discussion

The results are presented in three parts. First, the effect of mixing model to predict experimental trends is shown: we compare numerical predictions with the experimental trends in terms of the mass fraction of mono-particles produced as a function of blend strength and also as a function of percent excess HCl. We also discuss the effect of agglomeration. It will be shown that the proposed model is able to replicate experimentally observed trends, provided that mixing is not considered as perfect. The requirements for a more realistic agglomeration model are considered.

Then we explore the effects of process conditions. Given that mixing is not ideal, the distribution of particles throughout the vessel is provided as a function of flow rate and feed composition. This gives some initial insight into operations.

In the third part, the particle size distribution is analysed. Detailed comparison of the particle size distribution for both species and their evolution through the volume of the CIJR are shown. The implications of varying blend strength and percent excess HCl and the interactions between these two variables and the resulting PSDs are discussed.

As a summary, considerations on the model observations and their potential impact on operations are presented in the discussion section.

## Effect of local mixing

Experimental and numerical results for the production of mono- particles are compared in Fig. 6. Note that the experimental mass fraction of mono- (markers with fill) is based on elemental analysis. Numerical results (markers with no fill) are also given as the mass fraction of mono- particles relative to the total mass of particles produced. In the experiments, increasing the inlet concentration of MDA (blend strength) from 1 to 2 wt % leads to a shift from di- to mono- particle production (Fig. 6 (a)). The model trend correctly follows the experimental results. The shift from di- to mono- production occurs rapidly in experiments,

and happens more smoothly in the numerical results. The difference between the results is within 10% with the exception of one point at 2% MDA. A similar deviation is observed in Fig. 6 (b) where the effect of HCl excess on mono- production is given. The model captures complex experimental trends in this case as well. Given our limited knowledge of key physical constants for the system (see Table 3), these results are very promising.

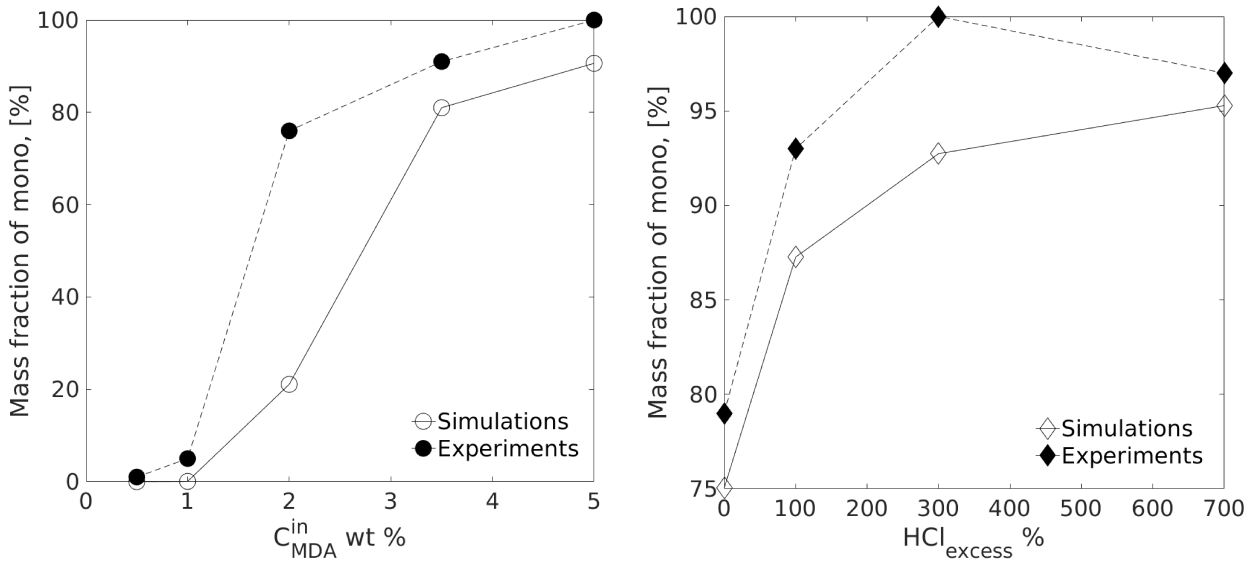


Figure 6: The mass fraction of mono- scaled to the total mass of particles produced at an inlet flow rate of $Q_{in} = 100$ ml/min as a function of (a) MDA inlet concentration at a fixed HCl excess of 300% and (b) as a function of HCl excess at $C^{in}_{MDA} = 5.0$ wt % shows a good agreement between model and experiments. An expanded scale is used in Fig. 6(b).

Agglomeration of particles is assessed next. The maximum size of agglomerates measured experimentally is 30 $\mu$m. This is the only data we have to guide our selection of the agglomeration efficiency ($\alpha$) of the particles. To show that the choice of $\alpha$ substantially affects the size of agglomerates, we performed simulations for the case characterized by the following set of process conditions: $Q_{in} = 50$ ml/min, $C^{in}_{MDA} = 0.5$ % wt, and $HCl_{excess} = 0\%$. In this case, only di- particles are produced. We first set $\alpha = 1$ meaning that all particle collisions result in agglomeration. The resulting particle size distribution is presented in Fig. 7.

With $\alpha = 1$, the simulation ended before the steady state because the maximum particle size permitted (30 $\mu$m) was exceeded. This shows that a simple model with 100% collision

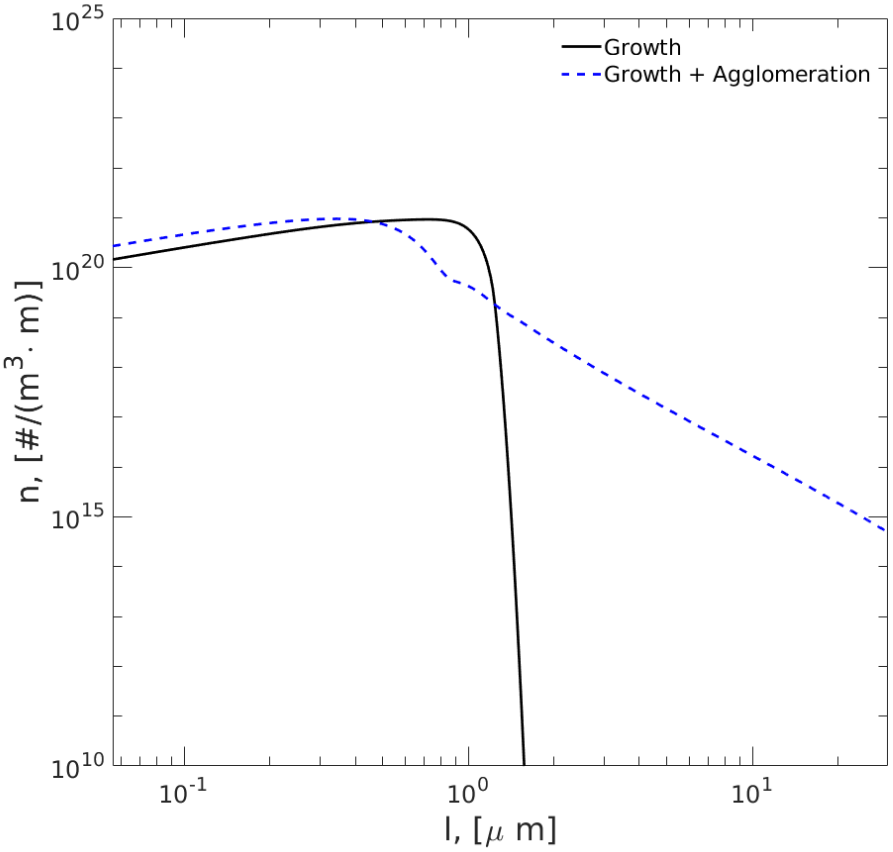


Figure 7: Di- particle size distribution for the case with process conditions: $Q_{in} = 50$ ml/min, $C^{in}_{MDA} = 0.5$ wt %, and HCl excess $- 0$ %. The results for pure growth and growth + agglomeration are shown.

efficiency cannot correctly predict agglomeration. The model predicts experimental trends correctly with growth alone suggesting that agglomeration affects the particle size distributions but not the composition of the product. The rest of the results in this paper present the case with growth alone.

Experiments showed a clear shift from di- to mono- particle production but the reason for this shift was not clear. The next set of simulations was designed to probe the effect of mixing on product composition at varying feed concentrations. As outlined in Fig. 2, there are numerous interrelated physical phenomena occurring simultaneously. A way to substantially modify model complexity is by changing the level of resolution of the flow. A straightforward simplification is to assume perfect mixing in the CIJR, i.e. once the round

jets collide, they mix perfectly throughout the entire reactor. To check if perfect mixing can be assumed to model the system under consideration, we removed the mixing model and ran simulation cases for the simplified case of perfect mixing. The model predictions with perfect mixing at $Q_{in} = 50$ ml/min are shown in Fig. 8. The main objective of Fig. 8 is to show the impact of the mixing model on the ability of the mechanistic model to predict the major experimental trend which is the shift from di- to mono- particle production with increase of the blend strength. To facilitate the visualization of this shift, the mass fraction of mono- (markers with no fill) and the mass fraction of di- (markers with the fill) are both depicted on each plot as functions of the blend strength (inlet concentration of MDA). The increasing HCl excess is shown by arrows.

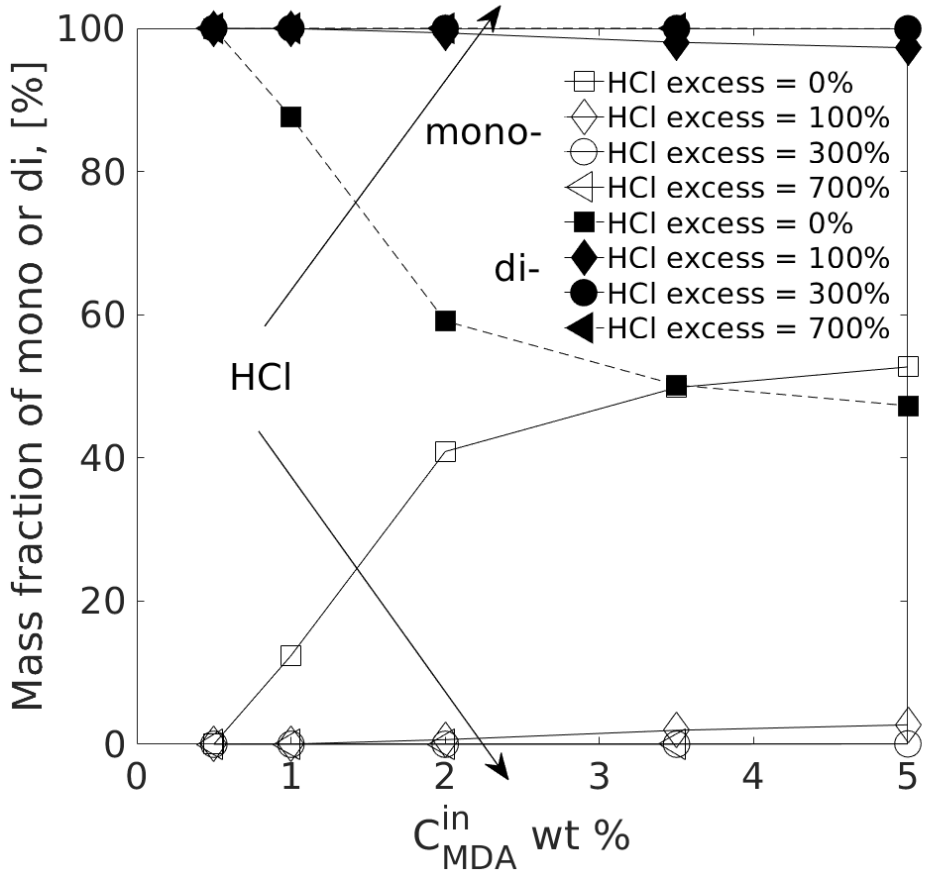


Figure 8: Mass of mono- or di- particles scaled to the total mass of particles produced at inlet flow rate of $Q_{in} = 50$ ml/min and different HCl excess values as a function of the blend strength with perfect mixing assumption.

The mixing model has a dramatic impact on the quality of the prediction. When there is no excess HCl and mixing is perfect (Fig. 8), the production of di- decreases with the increase of $C^{in}_{MDA}$ meaning that more mono- is produced at the higher blend strength (almost 50/50 ratio at $C^{in}_{MDA} = 5.0$ wt %). This can be explained by the fact that there is not enough HCl to react with mono- to produce di-. As the HCl excess increases under perfect mixing conditions, the production of di- increases drastically: mono- instantaneously reacts with HCl producing di- such that even at $C^{in}_{MDA} > 2$ wt % *there is no shift from di- to mono- production.* This result is at odds with the experimental results shown in Fig. 6. We conclude that perfect mixing cannot be assumed in CIJR, for the materials and process conditions considered in this work. The mixing model is needed to capture sensitivity to local mixing conditions resulting from the competitive-consecutive nature of the two chemical reactions.

## Effect of process conditions

Model predictions for the same flow conditions as Fig. 8 ($Q_{in} = 50$ ml/min) and varying $HCl_{excess}$ with the full mixing model are shown in Fig. 9, where the mass fraction of mono- and di- particles is plotted as a function of $C^{in}_{MDA}$. The shift from di- to mono- production occurs for all values of HCl, and as $HCl_{excess}$ increases the shift is more abrupt. Similar results were obtained for the other two values of the inlet flow rate. With an increase of the inlet flow rate $Q_{in}$ to 100 ml/min and 150 ml/min (not shown), overall trends are the same and the shift occurs at higher values of the blend strength (in the range 2 to 3.5 wt %). This mixing model is able to accurately replicate experimental observations.

In Table 4 the mass fraction of mono- and di- particles in the radial jet and in the bulk is given.

Mass fractions of mono- and di- in the radial jet and in the bulk show the distribution of particles in the vessel. More particles precipitate in the radial jet with an increase in the amount of reagents fed (increased blend strength and/or HCl excess). An increase in the inlet flow rate results in a slight decrease of particle production due to the reduction

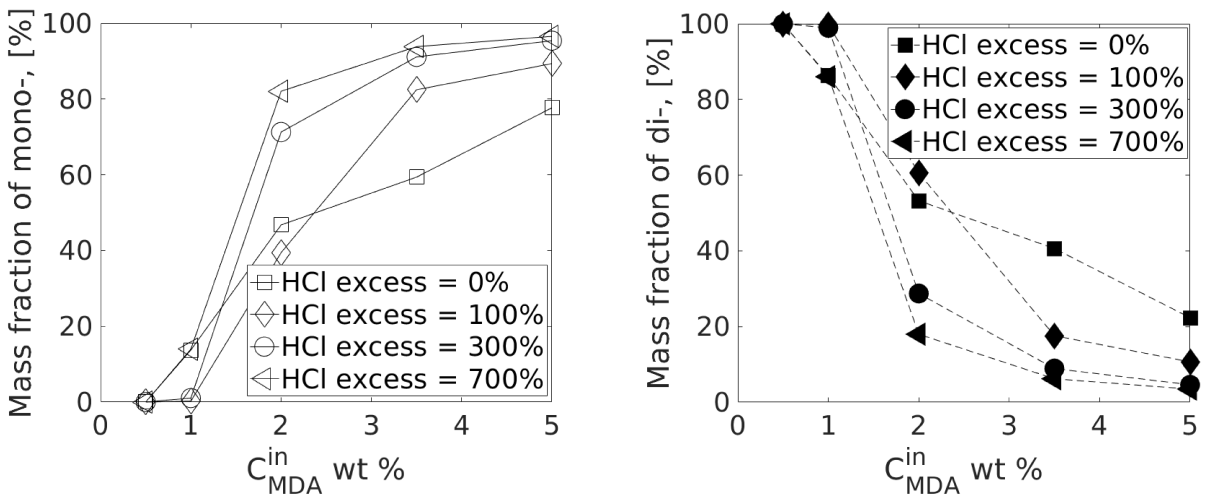


(a) Mono- (b) Di-

Figure 9: Mass of mono- or di- particles scaled to the total mass of particles produced at inlet flow rate of $Q_{in} = 50$ ml/min and different HCl excess values as a function of the blend strength with the radial jet mixing model.

in residence time. Note that the radial jet is a combination of fresh feed, production, and entrained particles from the bulk, so the mass fraction of particles is always lower in this part of the vessel.

## Analysis of the particle size distribution

The mechanistic model also predicts the full particle size distributions (PSDs) in different regions of the reactor (99×2 compartments in the radial jet + 1 in the bulk).

It is important to highlight that neither the experimental campaign nor the industrial partners could produce AHC salts PSDs, therefore, the model predictions with respect to the full PSDs presented hereafter are presented without validation. This lack of data is clearly one of the limitations of working with industrially relevant materials rather than model materials. The goal of the model is to uncover the role of the process variables on the production of the salts and variation of the PSDs in order to identify next steps in expanding our understanding of this difficult process. Readers who may be familiar with industrial operations will know that production of fine particles is a desireable state for

Table 4: Results of the simulations in terms of the distribution of particles (mass fractions) in the vessel at flow rates 50 and 150 ml/min and varying blend strength and HCl excess. Trends are the same for $Q_{in} = 100$ ml/min.

| Inlet flow rate, $Q_{in}$ ml/min | HCl excess, % | $C^{in}_{MDA}$, wt % | Jet, wt % | | Bulk, wt % | |
|---|---|---|---|---|---|---|
| | | | mono | di | mono | di |
| 50 | 0 | 0.5 | 0.0 | 9.1 | 0.0 | 90.9 |
| | | 1.0 | 1.2 | 7.8 | 12.5 | 78.5 |
| | | 2.0 | 4.3 | 4.9 | 42.5 | 78.5 |
| | | 3.5 | 5.5 | 3.7 | 53.9 | 36.9 |
| | | 5.0 | 7.5 | 2.0 | 70.2 | 20.3 |
| | 700 | 0.5 | 0.0 | 9.1 | 0.0 | 90.9 |
| | | 1.0 | 1.6 | 7.9 | 12.4 | 78.1 |
| | | 2.0 | 15.5 | 2.1 | 66.5 | 15.9 |
| | | 3.5 | 21.5 | 0.8 | 72.3 | 5.4 |
| | | 5.0 | 23.5 | 0.4 | 73.1 | 3.0 |
| 150 | 0 | 0.5 | 0.0 | 9.2 | 0.3 | 90.5 |
| | | 1.0 | 0.6 | 8.5 | 6.0 | 84.9 |
| | | 2.0 | 5.8 | 3.3 | 58.4 | 32.5 |
| | | 3.5 | 6.7 | 2.4 | 66.8 | 24.1 |
| | | 5.0 | 7.0 | 2.2 | 69.5 | 21.3 |
| | 700 | 0.5 | 0.0 | 9.0 | 0.0 | 91.0 |
| | | 1.0 | 0.0 | 9.1 | 0.0 | 90.9 |
| | | 2.0 | 6.0 | 4.3 | 47.3 | 42.4 |
| | | 3.5 | 14.9 | 1.2 | 72.6 | 11.3 |
| | | 5.0 | 18.7 | 0.6 | 75.1 | 5.6 |

re-dissolution if the solubility is high. In cases like this, where the by-product solubility is relatively low, dissolution may not occur and the resulting large numbers of fine particles can be very difficult to process. To this end, the PSDs predicted by the model are discussed in terms of trends and controlling variables.

The spatial development of the PSDs in compartments of the radial jet for the '$a$' and '$b$' sides separated into mono- and di- particles is shown in Fig. 10 for $Q_{in} = 50$ ml/min. The arrows indicate the PSDs starting from compartment 1 to 99, as the radial jet expands from the impingement point in the radial direction.

Starting from the first compartment right after the impingement point, the PSD in every $7^{\text{th}}$ compartment is shown (i.e. 1, 8, 15, ..., 99). The limiting values of the process variables

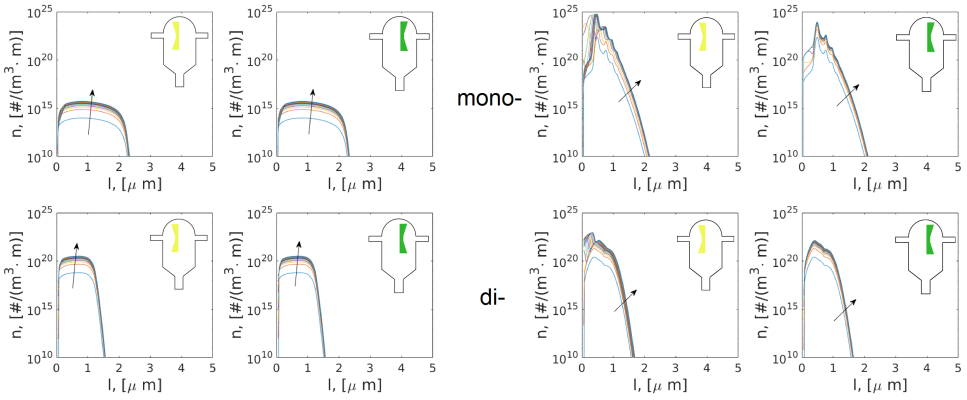


(a) Low $C^{in}_{MDA}$ – Low $HCl_{excess}$ (b) High $C^{in}_{MDA}$ – High $HCl_{excess}$

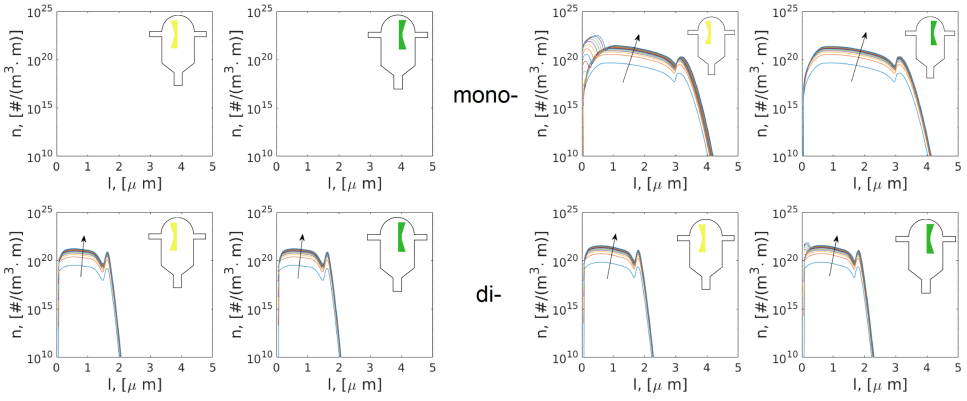


(c) Low $C^{in}_{MDA}$ – High $HCl_{excess}$ (d) High $C^{in}_{MDA}$ – Low $HCl_{excess}$

Figure 10: Spatial development of PSDs in the **jet** at $Q_{in} = 50$ ml/min separated into mono- and di- particles. Low and high correspond to the lowest and highest values of the process conditions: (a) $C^{in}_{MDA} = 0.5$ wt % (low), $HCl_{excess} = 0$ % (low); (b) $C^{in}_{MDA} = 5.0$ wt % (high), $HCl_{excess} = 700$ % (high); (c) $C^{in}_{MDA} = 0.5$ wt % (low), $HCl_{excess} = 700$ % (high); (d) $C^{in}_{MDA} = 5.0$ wt % (high), $HCl_{excess} = 0$ % (low).

are presented in the following way: 'Low' refers to $C^{in}_{MDA} = 0.5$ wt % or $HCl_{excess} = 0$ %, 'High' denotes $C^{in}_{MDA} = 5.0$ wt % or $HCl_{excess} = 700$ %. All four combinations of these variables are shown.

The process variables significantly interact and affect the shape of the PSDs. Low values of process variables (Fig. 11(a)) produce a small number of small particles (mass of mono- is negligibly small).

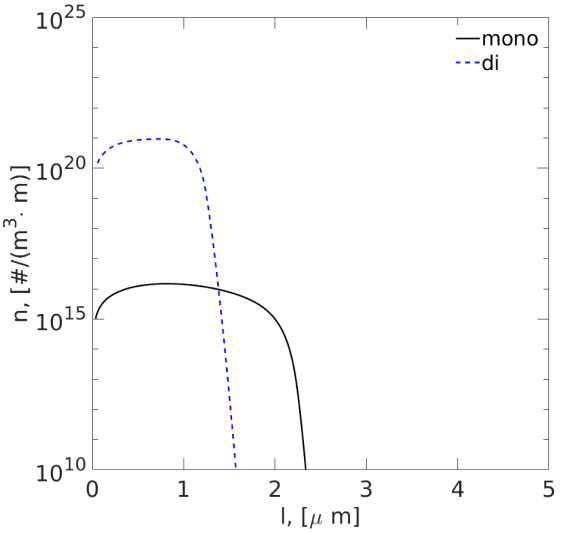


(a) Low $C^{in}_{MDA}$ – Low $HCl_{excess}$

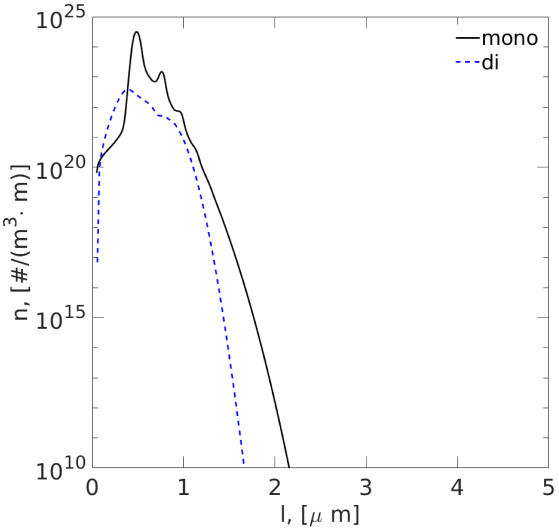


(b) High $C^{in}_{MDA}$ – High $HCl_{excess}$

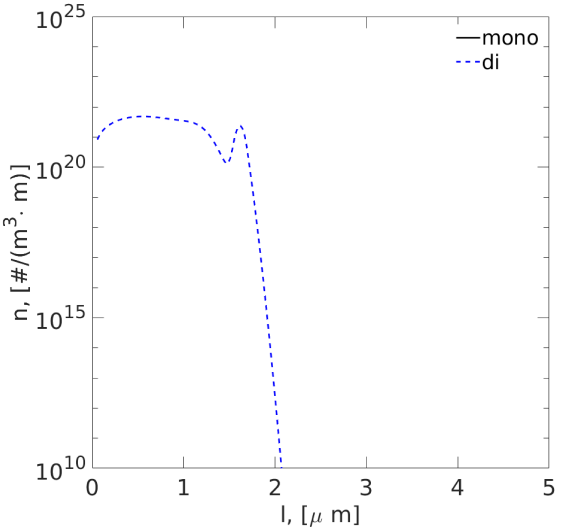


(c) Low $C^{in}_{MDA}$ – High $HCl_{excess}$

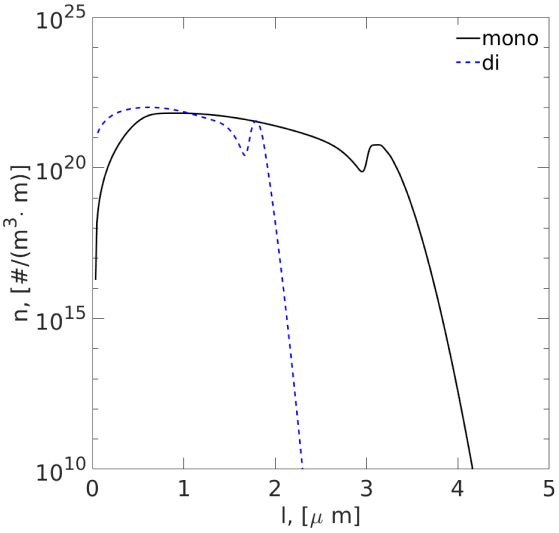


(d) High $C^{in}_{MDA}$ – Low $HCl_{excess}$

Figure 11: PSDs of mono- and di- particles in the **bulk** at $Q_{in} = 50$ ml/min. Low and high correspond to the lowest and highest values of the process conditions: (a) $C^{in}_{MDA} = 0.5$ wt % (low), $HCl_{excess} = 0$ % (low); (b) $C^{in}_{MDA} = 5.0$ wt % (high), $HCl_{excess} = 700$ % (high); (c) $C^{in}_{MDA} = 0.5$ wt % (low), $HCl_{excess} = 700$ % (high); (d) $C^{in}_{MDA} = 5.0$ wt % (high), $HCl_{excess} = 0$ % (low).

High blend strength and HCl excess result in a large number of small particles (Fig. 11(b)). At low $C^{in}_{MDA}$ and high HCl excess (Fig. 11(c)) only di- particles are produced in relatively small amount. High blend strength and low HCl excess (Fig. 11(d)) noticeably broaden the

PSD and produce particles of larger size. In all cases, the maximum size of mono- particles is larger than of di- which matches experimental data.

The shape of the PSD loses its symmetry around the impingement plane ('$a$' and '$b$' sides of the radial jet) at high values of the process variables due to changes in local concentrations (HCl-rich versus MDA-rich). When the blend strength is high, more small mono- (and di-) particles are produced at the '$a$' side (see Fig. 10 (b) and (d) left set). At high $C^{in}_{MDA}$ and low $HCl_{excess}$, a slight increase of the production of small di- particles is seen (Fig. 10 (d)).

The first compartment of the radial jet has a volume of $2.28 \cdot 10^{-2}$ ml and the residence time is $2.74 \cdot 10^{-2}$ s at a flow rate of $Q_{in} = 50$ ml/min. As the process moves from the impingement point along the radial jet, more particles are produced and they grow in size. After the last radial jet compartment, the particles are released into the bulk.

Fig. 11 shows the PSDs of mono- and di- particles in the bulk for the same four process conditions as shown in Figure 10 for the radial jet. The PSD in the first compartment in the radial jet also defines the shape of the PSD in the bulk. Due to the larger residence time in the bulk, particles have more time to grow, resulting in slightly wider PSDs than in the radial jet. In comparing Fig. 10 and Fig. 11, we conclude that it is primarily the local conditions of the process variables at the impingement point which defines the shape of the PSD in the bulk.

## Discussion

The results of the model (Fig. 10 and 11) guide us in selecting process conditions to either minimize the production of the particles or decrease the reprocessing costs. The highest values of the process variables lead to production of the largest amount of smaller particles of both types (Fig. 11 (b)). This case is considered as the most favorable: since particles are small, they will dissolve faster; the size of both particle types is the same, thus, the same reprocessing approach can be applied. An alternate condition is low blend strength and high HCl excess (Fig. 11 (c)). In this case, a relatively small number of di- particles is produced, i.e. small particles of one type (less than half of the amount than in the previous

case). The worst case scenario is high blend strength combined with the low HCl excess. In this case, a large number of bigger particles of both types is generated. Between the two process variables: the blend strength ($C^{in}_{MDA}$) and the HCl excess ($HCl_{excess}$); the former dominates the type of the particles being produced while the later affects the number. It is also noted that di- particles are consistently smaller than mono- particles which is consistent with experimental results (see ref.[3]).

The mechanistic model has allowed us to study the effect of process conditions on the particle size distribution. The influence of the blend strength on the PSD at two limiting values of HCl excess for $Q_{in} = 50$ ml/min is shown in Fig. 12 for mono- (left) and di- (right) particles in the bulk.

At low HCl excess, low $C^{in}_{MDA}$ means less by-product formation and low overall production of particles. As $C^{in}_{MDA}$ increases, the production of particles increases. There is a noticeable transition in the shape of the distributions with the increase of the blend strength at high HCl excess. This transition is quite sudden (not smooth). In all cases, it is complete by 2 wt % which is consistent with the shift of di- to mono- production that happens at blend strength values in the range 1 to 2 wt %. The same is true at low % excess HCl, but is somewhat less pronounced. Based on these results, we conclude that variation of the blend strength is the most efficient means to control local concentration of reacting species, and, therefore, the production of mono- and di- particles.

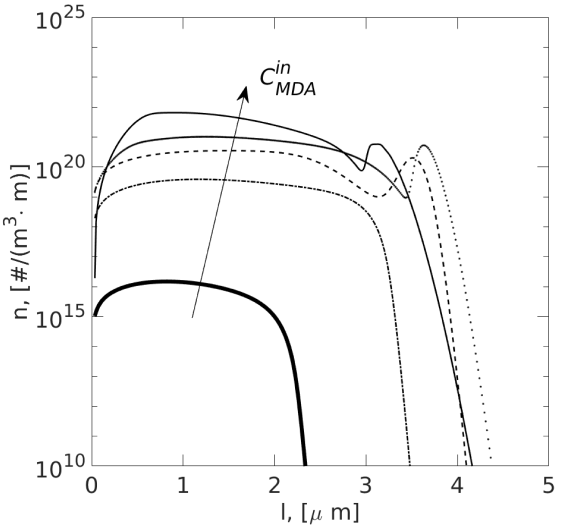


(a) Low $HCl_{excess}$ mono-

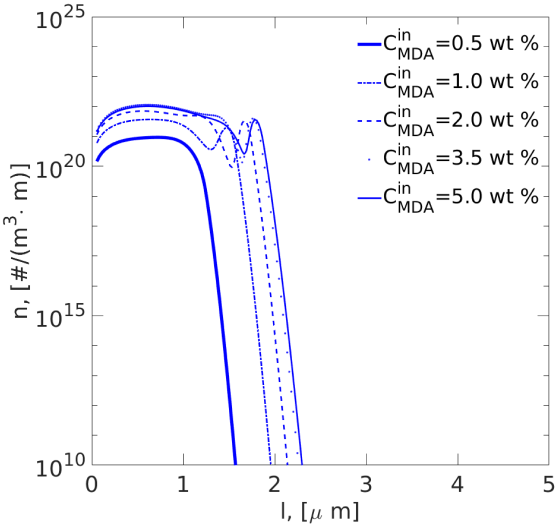


(b) Low $HCl_{excess}$ di-

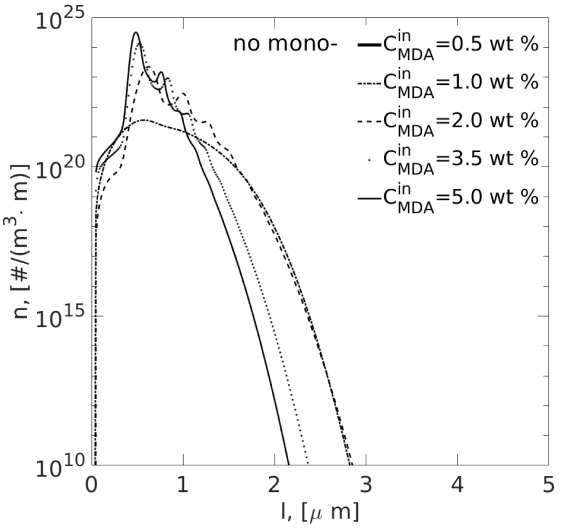


(c) High $HCl_{excess}$ mono-

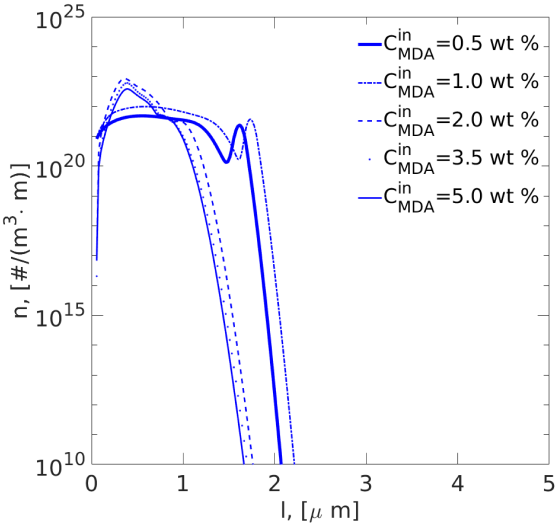


(d) High $HCl_{excess}$ di-

Figure 12: PSD of mono- and di- particles in the bulk for for different blend strength values at $Q_{in}$ = 50 ml/min: (a) mono- and (b) di- at $HCl_{excess}$ = 0 %; (c) mono- and (d) di- at $HCl_{excess}$ = 700 %.

# Conclusions

A mechanistic model to describe the production of amine hydrochloride salts (mono- and di-) in a confined impinging jet reactor (CIJR) is reported. The model couples population

balance equations (PBEs) that track the particle size distributions (PSDs) with equations for chemical reaction kinetics, nucleation, particle growth, agglomeration, and a mixing model that accounts for spatial inhomogeneity of the flow and concentration within the CIJR. The numerical schemes and computational methods for the solution of the model are presented in detail, verified, and validated by comparison of the numerical results with experiments.

The mechanistic model proved to be successful in predicting major experimental results. The key finding of this study is that perfect mixing cannot always be assumed in the CIJR. Based on the fundamental equations that govern the development of the radial jet as a result of a collision of two round jets, a mixing model was derived that is the core element of the mechanistic model. The mixing model must be included in order to predict the shift from di- to mono- particle production as the inlet concentration of MDA (blend strength) increases past 2%. In experiments, this shift occurs abruptly when $C^{in}_{MDA}$ is in the range 1 to 2 wt % and is independent of the inlet flow rate value $Q_{in}$ and HCl excess $HCl_{excess}$. In numerical simulations, the shift is smooth and occurs over a wider range of the blend strength $(1-3.5)$ wt %. This difference could be due to a non-optimal choice of the physical constants of the model that were determined in our earlier publication[20], or it could be due to the limited number of experiments that were available to define the experimental curve.

The mechanistic model predicts full particle size distributions in different regions of the reactor. The shape of the PSD is shown to be set in the localized region near the impingement point. The PSD shape undergoes minor changes as the reactants flow from the radial jet to the bulk. These changes are defined by the growth of the particles. The blend strength $C^{in}_{MDA}$ strongly affects the shape of the PSD which changes suddenly as $C^{in}_{MDA}$ passes 2 wt %. The percent excess HCl influences the amount of particles being produced and has minor affect on the shape of the PSD.

One of the main goals of the model is its ability to outline the process conditions such that the production of the salts is either mitigated or well controlled. Based on our results, we conclude that high values of the blend strength and the HCl excess lead to the production

of large amount of small particles of both types which may lead to faster re-dissolution and similar reprocessing treatments.

## Acknowledgement

The financial support provided by Huntsman International is gratefully acknowledged. The authors thank Archie Eaglesham, Don Jones, Neal Grob and Wayne Anthon for helpful discussions about AHC salts behaviour at production scale that facilitated understanding of the lab-scale process and development of a mechanistic model. F. Maluta acknowledges the 'Ing.Toso Montanari' Foundation for his scholarship.

## Supporting Information

The details of discretization of population balance equations and verification and validation of the numerical scheme is provided in Supporting Information. This information is available free of charge via the Internet at http://pubs.acs.org/

# Nomenclature

$(\Delta)$ $x$ coordinate where the maximum $x$-velocity is equal to $v_0$, [m]

$\bar{v}_x(x)$ y-average of the downstream velocity, [m/s]

$\dot{n}'''_{i,g,a}$ rate of generation of the $i^{th}$ component per unit volume, [mol/(s $\cdot$ m$^3$)]

$\dot{V}$ Volumetric flow rate, [m$^3$/s]

$\dot{V}_E$ Engulfment volumetric flow rate, [m$^3$/s]

$\dot{V}_e$ Volumetric flow rate discharged from the radial jet in the bulk, [m$^3$/s]

$\dot{V}_u$ Volumetric flow rate exiting the reactor, [m$^3$/s]

$\ell$ Characteristic diameter of the solid particles, mono- or di-, [m]

$\eta$ Non-dimensional constant containing both $x$ and $y$, [$-$]

$\Omega$ Depth of the control volume along the $\omega$ axis, [rad]

$\phi$ Expansion angle of the radial jet, [°]

$\rho$ fluid density, [kg/m$^3$]

$\sigma_0^{-1}$ Spreading constant of the turbulent radial jet, [$-$]

$\tau_{bulk}$ Residence time in the bulk

$\theta$ Non-dimensional constant containing both $x$ and $y$, [$-$]

$b_0$ initial half width of the radial jet, [m]

$C$ Concentration

$C_i$ Concentration of the $i^{th}$ component in the bulk, [kmol/m$^3$]

$C_{i,a}$ molar concentration of the $i^{th}$ component in the semicompartment $a$, [kmol $\cdot$ m$^{-3}$]

$C_{i,b}$ molar concentration of the $i^{th}$ component in the semicompartment $b$, [kmol $\cdot$ m$^{-3}$]

$C_{i,E}$ molar concentration of the $i^{th}$ component engulfed from the bulk entering the semicompartment $a$, [kmol $\cdot$ $m^{-3}$]

$K_e$ kinematic momentum flux, [m$^4$/s$^2$]

$n_n(\ell)$ Number density of n-particles in the population for which the characteristic diameter takes a value of exactly $\ell$, [$\#/\mathrm{m}^3 \cdot \mathrm{m}$]

$S$ Supersaturation

$V$ volume of the differential element in the radial jet, [m$^3$]

$v_0$ Average velocity at the beginning of the radial jet

$v_E$ Engulfment velocity, [m/s]

$v_S$ Exchange velocity, [m/s]

$v_x$ Velocity in the $x$-direction, [m/s]

$V_{bulk}$ Volume of the bulk, [m$^3$]

$x_0$ Radius of the inlet round jets, [m]

$x_{max}$ Outer radius of the radial jet, [m]

$y^*(x)$ Width of the radial jet at the $x$ position, [m]

$Z$ fraction of the engulfment velocity that defines the exchange velocity, [$-$]

# References


(1) Tung, H.-H.; Paul, E. L.; Midler, M.; McCauley, J. *Crystallization of Organic Compounds: an Industrial Perspective*; John Wiley & Sons, Hoboken, New Jersey, 2009; Chapter 10, p. 207.

(2) Schwarzer, H.-C.; Peukert, W. Experimental Investigation into the Influence of Mixing on Nanoparticle Precipitation. *Chem. Eng. Technol.* **2002**, *25*, 657.

(3) Ershad, N. F. University of Alberta. Ph.D. thesis, University of Alberta, 2013.

(4) Marchal, P.; David, R.; Kelin, J.; Villermaux, J. Crystallization and Precipitation Engineering - I. An Efficient Method for Solving Population Balance in Crystallization with Agglomeration. *Chem. Eng. Sci.* **1988**, *43*, 59.

(5) Hounslow, J.; Ryall, R. L.; Marshall, V. R. A Discretized Population Balance for Nucleation, Growth, and Aggregation. *AIChE J.* **1988**, *34*, 1821.

(6) Kumar, S.; Ramkrishna, D. On the Solution of Population Balance Equations by Discretization - I. A Fixed Pivot Technique. *Chem. Eng. Res. Des.* **1996**, *51*, 1311.

(7) Zauner, R.; Jones, A. G. On the Influence of Mixing on Crystal Precipitation Processes — Application of the Segregated Feed Model. *Chem. Eng. Sci.* **2002**, *57*, 821.

(8) Kresta, S. M.; Anthieren, G.; Parsiegla, K. Mixing Effects in Silver Halide Precipitation. Linking Theory with Practice Using a Multi-Mechanism Model. *Chem. Eng. Res. Des.* **2004**, *82*, 1117.

(9) Kresta, S. M.; Anthieren, G.; Parsiegla, K. Model Reduction for Prediction of Silver Halide Precipitation. *Chem. Eng. Sci.* **2005**, *60*, 2135.

(10) Schwarzer, H.-C.; Peukert, W. Tailoring Particle Size Through Nanoparticle Precipitation. *Chem. Eng. Commun.* **2004**, *191*, 580.

(11) Schwarzer, H.-C.; Peukert, W. Combined Experimental/Numerical Study on the Precipitation of Nanoparticles. *AIChE J.* **2004**, *50*, 3234.

(12) Liu, Y.; Fox, R. O. CFD Predictions for Chemical Processing in a Confined Impinging-Jets Reactor. *AIChE J.* **2006**, *52*, 731.

(13) Gavi, E.; Marchisio, D. L.; Barresi, A. A. CFD Modelling and Scale-up of Confined Impinging Jet Reactors. *Chem. Eng. Sci.* **2007**, *62*, 2228.

(14) Marchisio, D. L. Large Eddy Simulation of Mixing and Reaction in a Confined Impinging Jets Reactor. *Comput. Chem. Eng.* **2009**, *33*, 408.

(15) Gavi, E.; Marchisio, D. L.; Barresi, A. A.; Olsen, M. G.; Fox, R. O. Turbulent Precipitation in Micromixers: CFD Simulation and Flow Field Validation. *Chem. Eng. Res. Des.* **2010**, *88*, 1182.

(16) Makowski, Ł.; Orciuch, W.; Baldyga, J. Large Eddy Simulations of Mixing Effects on the Course of Precipitation Process. *Chem. Eng. Sc.* **2012**, *77*, 85.

(17) Metzger, L.; Kind, M. The Influence of Mixing on Fast Precipitation Processes – A Coupled 3D CFD-PBE Approach Using the Direct Quadrature Method of Moments (DQMOM). *Chem. Eng. Sci.* **2017**, *169*, 284.

(18) Cheng, J.; Yang, C.; Mao, Z.-S. CFD-PBE Simulation of Premixed Continuous Precipitation Incorporating Nucleation, Growth and Aggregation in a Stirred Tank with Multi-Class Method. *Chem. Eng. Sci.* **2012**, *68*, 469.

(19) Siddiqui, S. W. Use of the Confined Impinging Jet Reactor for Production of Nanoscale Iron Oxide Particles. Ph.D. thesis, University of Alberta, 2009.

(20) Maluta, F.; Eaglesham, A.; Jones, D.; Komrakova, A.; Kresta, S. M. A Novel Factorial Design Search to Determine Realizable Constant Sets for a Multi-Mechanism Model of Mixing Sensitive Precipitation. *Comput. Chem. Eng.* **2017**, *106*, 322.

(21) Mersmann, A., Ed. *Crystallization technology handbook*, 2nd ed.; Marcel Dekker, Inc.: New York, Basel, 2001; p 832.

(22) Eitzlmayr, A.; Petschacher, C.; Radl, S.; Suzzi, D.; Zimmer, A.; Khinast, J. G. Modeling and Simulation of Polyacrylic Acid/Protamine Nanoparticle Precipitation. *Soft Matter* **2011**, *7*, 9484.

(23) Gavi, E.; Rivautella, L.; Marchisio, D.; Vanni, M.; Barresi, A.; Baldi, G. CFD Modelling of Nano-Particle Precipitation in Confined Impinging Jet Reactors. *Chem. Eng. Res. Des.* **2007**, *85*, 735.

(24) Schwarzer, H.-C.; Schwertfirm, F.; Manhart, M.; Schmid, H.-J.; Peukert, W. Predictive Simulation of Nanoparticle Precipitation Based on the Population Balance Equation. *Chem. Eng. Sci.* **2006**, *61*, 167.

(25) Siddiqui, S. W.; Zhao, Y.; Kukukova, A.; Kresta, S. M. Characteristics of a Confined Impinging Jet Reactor: Energy Dissipation, Homogeneous and Heterogeneous Reaction Products, and Effect of Unequal Flow. *Ind. Eng. Chem. Res.* **2009**, *48*, 7945.

(26) Hunt, G. R.; Ingham, D. B. Laminar and Turbulent Radial Jets. *Acta Mechanica* **1998**, *127*, 25.

(27) Schlichting, H. *Boundary Layer Theory.*; McGraw-Hill: New York, 1960.

(28) Vale, H.; McKenna, T. Modeling Particle Size Distribution in Emulsion Polymerization Reactors. *Prog. Polym. Sci.* **2005**, *30*, 1019.

(29) Gunawan, R.; Fusman, I.; Braatz, R. D. High Resolution Algorithms for Multidimensional Population Balance Equations. *AIChE J.* **2004**, *50*, 2738.

(30) Bouaswaig, A. E.; Engell, S. Comparison of High Resolution Schemes for Solving Population Balances. *Ind. Eng. Chem. Res.* **2010**, *49*, 5911.

(31) Hermanto, M. W.; Braatz, R. D.; Chiu, M.-S. High-Order Simulation of Polymorphic Crystallization Using Weighted Essentially Nonoscillatory Methods. *AIChE J.* **2009**, *55*, 122.

(32) Shu, C. W.; Osher, S. Efficient Implementation of Essentially Non-Oscillatory Shock-Capturing Schemes. *J. Comput. Phys.* **1988**, *77*, 439.

(33) Shu, C.-W.; Osher, S. Efficient Implementation of Essentially Non-Oscillatory Shock-Capturing Schemes, II. *Comp. Phys.* **1989**, *83*, 32.

(34) Henrick, A. K.; Aslam, T. D.; Powers, J. M. Mapped Weighted Essentially Non-Oscillatory Schemes: Achieving Optimal Order Near Critical Points. *J. Comput. Phys.* **2005**, *207*, 542.

(35) Icardi, M.; Gavi, E.; Marchisio, D. L.; Barresi, A. A.; Olsen, M. G.; Fox, R. O.; Lakehal, D. Investigation of the flow field in a three-dimensional Confined Impinging Jets Reactor by means of microPIV and DNS. *Chem. Eng. J.* **2011**, *166*, 294.

# Graphical TOC Entry